INVESTIGATION FLAPPING-FLIGHT AERODYNAMICS OF A ROBOTIC BIRD

H.W.M. Hoeijmakers[1], L.H. Groot Koerkamp[1,2], L.D. de Santana[1], C.H. Venner[1], S. Stramigioli[2], J.L. Mulder[1], A. Brentjes[1], F. Gijsman[1], S.A. Hartman[1]

[1]Group Engineering Fluid Dynamics, University of Twente, P.O. Box 217, 7500 AE Enschede, the Netherlands
[2]Group Robotics and mechatronics, University of Twente, P.O. Box 217, 7500 AE Enschede, the Netherlands

Abstract

The Robird is a bird-like drone or ornithopter that generates both lift and thrust by flapping its wings. Its appearance, size and weight, but specifically its flapping flight performance resemble that of a Peregrine falcon. This paper describes an extension of Prandtl's Lifting-line method from steady flow to unsteady flow to predict the unsteady lift and thrust of the robotic bird. The extension comprises the derivation of the Kutta-Joukowski Theorem for unsteady flow, an unsteady Kutta condition and the representation of the wake as a stationary transpiration surface carrying a time-dependent dipole distribution, which instantaneous strength is solved from the spanwise distribution of the circulation of the lifting line at earlier times. For the cases considered, the numerical method predicts that both the section-lift and section-thrust of the wing vary with time. The cycle-averaged section-lift and section-thrust, as well as the cycle-averaged overall lift and thrust, are mostly positive during the flapping flight. Cycle-averaged distributions of sectional circulation, lift and upwash, as well as cycle-averaged overall lift depend on Strouhal number, not on pitch amplitude, while the distribution of cycle-averaged sectional thrust, as well as cycle-averaged overall thrust depend on Strouhal number and on pitch amplitude. The topology of the wake as predicted by the unsteady-lifting-line method, is compared to results of experiments performed with 2D3C PIV applied to a wind-tunnel model including a full-scale port-side wing of the Robird. For the downstroke, the near-wake of the flapping wing is a free shear layer, which vorticity distribution has the orientation as predicted by the vortex distribution determined by the unsteady-lifting-line method The results of the measurements and of the predictions show topological similarities.

Keywords: unsteady flow, aerodynamics of birds, lifting-line method, unsteady Kutta condition, PIV measurements

1. Introduction

The Robird [1] is an ornithopter-type of drone developed by Clear Flight Solutions (CFS) that was designed to appear like a Peregrine falcon during its flight, see Fig. 1. The drone has the same dimensions and weight as the life falcon, and produces lift and thrust by flapping its wings. Birds instinctively sense that a falcon in flapping flight is on the hunt, making the Robird very suitable for bird control at airports, garbage dumps, crop fields, etc. Its foam wings render the Robird different from ornithopters of similar size with foil-type rather than airfoil-type wings, such as the Robo Raven [2].
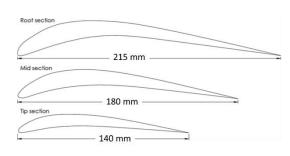

Figure 1 – Robird [1]: Design robotic bird based on Peregrine falcon (left). Typical airfoil sections wing Robird. (right).

Furthermore, the Robird wings do not pitch passively nor consist of hinged individually moving parts like the Festo Smartbird [3]. The size of these drones is in a different class than successful flapping Micro-Aerial Vehicles (MAV's), such as the Delfly [4] and the insect-sized robotic fly [5].

The performance of flapping wings is dominated by unsteady flow phenomena, which makes the aerodynamics inherently complex. Experimental work on birds and bird-like flapping wings has shown the importance of mechanisms such as leading-edge vortices for slow flight and hovering flight [6–8]. The challenge of formulating an aerodynamic model for flapping wings is to account for the dynamics of the wake in order to accurately predict the aerodynamic performance [9]. Many models for the wake have been proposed in the past [10], [11] and [12]. The results of these models share one important characteristic: the generation of thrust is associated with a wake that induces a jet-like flow. This jet-like flow has been confirmed to be present in the wake of the Robird with both numerical methods [13] and experimental methods [14] and [15]. The model of the wake to apply may depend on the bird species, and may even vary with flight speed for specific birds [16]. The accuracy of the wake models is influenced significantly by vortex dynamics, which makes the prediction of lift and drag sensitive to vortex dynamics [17].

Though the Robird proves that flapping flight by a robotic bird is possible, the theory behind the aerodynamics of flapping flight is not yet fully understood. The goal of the present study, carried out since 2012, is to contribute to a better understanding of the aerodynamics of flapping wing propulsion of a robotic bird like the Peregrine-falcon based Robird. In [18] the lift curve has been measured of a scale model of the wing of the Robird in order to obtain the lift and drag polar for steady, non-flapping flow conditions. This established the basic aerodynamics of the wing, with its highly cambered thin airfoil sections (similar to the ones of flying machines in the early part of last century), see Fig. 1, for the robotic bird operating at Reynolds numbers in the range of 30×10^4 to 10^5. CFD analysis [13] performed for 2D flow about the heaving/pitching Robird airfoils shown in Fig. 1, gave first insight in the unsteady aerodynamics of such cambered airfoils, as well as the relation between the flow in the wake and the generation of thrust. Further experimental studies [14], [15] and [19] focused on the wake downstream of a (full-scale) half-model of the Robird during flapping motion, using: (i) a wake rake, as well as a 5-hole probe; (ii) flow visualization, and; (iii) PIV (Particle Image Velocimetry) measurements, respectively. In [19] a simple unsteady potential flow model for 2D heaving/pitching motion has been presented developed for investigating whether a representation of the wake of a flapping wing by a vortex sheet results in the jet-like type of distribution of the axial velocity, generated by a reverse von Kármán vortex street. Such a velocity distribution in the wake is indicative for the generation of thrust by a flapping wing.

For the subsequent experimental part of the study an advanced PIV set-up has been designed and realized for the upgraded Aeroacoustic Wind Tunnel [20] at the University of Twente (open-jet test section $w \times h = 0.9\text{m} \times 0.7\text{m}$). In [21] the PIV campaign to obtain wake velocity data for the wake of the Robird port-side wing has been pursued further. In addition, an unsteady lifting-line method has been developed for the 3D flow about flapping wings.

The goal of the present study is to apply the unsteady lifting-line method to the Robird flapping motion in order to analyse its aerodynamics. Furthermore, numerical results are compared to results of new PIV measurements in the wake of the wind-tunnel model of the Robird.

The present paper is structured as follows: Section 2 introduces the Robird, the kinematics of the flapping wing of the Robird and the simplifications that will be made for the computational part of this study. Section 3 describes the computational method followed by section 4 with a description on how the developed lifting-line method for unsteady flow is applied to the Robird. This section is followed by section 5 which describes the experimental methodology. Finally, the results of the numerical method and of the experiment are compared in section 6, followed by the conclusions of the present investigation in section 7.

2. Kinematics Flapping Motion Wing Robotic Bird

The motion of a bird has many degrees of freedom. In the present study the description of the motion of the wings is restricted to the motion of a rigid wing with just two degrees of freedom: flapping $\gamma(t)$ and pitching $\theta(t)$. In a 2D frame work, the motion of a section of the wing is equivalent to a heaving $\dot{h}(t)$ pitching $\theta(t)$ motion, see Fig. 2.
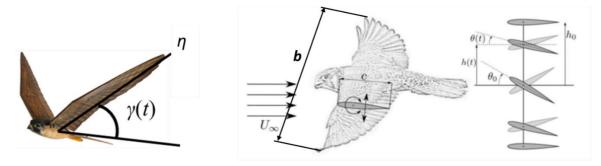
Figure 2 – Flapping/pitching motion of bird wings [13]. Left: definition flapping motion. Center Free stream and overall dimensions. Right: definition of equivalent 2D heaving/pitching motion airfoil sections.

The flapping motion $\gamma(t)$ is approximated as a harmonic motion of constant frequency, defined by

$$\gamma(t) = \gamma_1 + \gamma_0 \sin 2\pi \frac{t}{T}, \tag{1}$$

with $\gamma(t)$ the wing shoulder angle of the pitch axis as function of time, γ_0 is the amplitude of the flapping motion and γ_1 is the zero-position (off-set) of the wing. The period T of the motion equals $T = 1/f$, with f the frequency of the flapping motion. The pitching motion, coupled to the plunging motion, is a harmonic motion of the same frequency, defined as

$$\theta(t) = \theta_1 + \theta_0 \sin\left(2\pi \frac{t}{T} + \phi\right), \tag{2}$$

with $\theta(t)$ the pitching angle around the pitch axis as function of time, θ_0 the amplitude of the pitch, θ_1 the off-set of the pitch angle and ϕ the phase shift between flapping motion and pitching motion. It is assumed that all motion parameters, i.e., γ_0, γ_1, θ_0, θ_1 and ϕ are constant along the pitch axis. Note that here the pitch angle θ does not depend on the spanwise coordinate η, i.e., nor geometric twist, nor aerodynamic twist, due to the flexibility of the wing, is considered. Furthermore, also the zero-lift angle of attack α_0 of the airfoil sections is assumed to have a constant value along the entire span of the wing. Therefore, since the parameter α_0 represents the effect of the camber of the airfoil sections on the lift curve, the variation of the airfoil sections along the span is neglected, only a single, representative, value of the zero-lift angle of attack α_0 is taken into account.

The height $h(t)$, above the horizontal plane, of the ¼-chord point of the airfoil section at distance y from the pivotal point of the plunging motion, is a function of γ_0 and γ_1:

$$h(y,t) = y \sin\gamma(t), \text{ for } y \in [-b/2, b/2], \tag{3}$$

with b the full span of the wing.

In the lifting-line method to be discussed, the boundary conditions are applied on a stationary reference surface, here the plane $z = 0$. The effect of the motion of the wing is accounted for through the so-called effective angle of attack $\alpha_{eff}(y,t)$ of the airfoil sections along the span of the wing, see Fig. 3:

$$\alpha_{eff}(y,t) = \theta(t) + \arctan\left(\frac{-1}{U_\infty} \frac{\partial h(y,t)}{\partial t}\right). \tag{4}$$
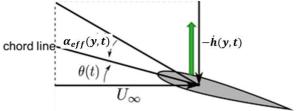

Figure 3 – Effective angle of attack $\alpha_{eff}(y,t)$ due to plunging/pitching motion. Green arrow indicates direction of plunging motion. Angle of attack due to plunging motion equals $\alpha_{plunge} = \arctan\left(\frac{-1}{U_\infty} \frac{\partial h(y,t)}{\partial t}\right)$.

The contribution of the plunge (heave) of the airfoil sections due to the flapping motion of the wing follows from the time variation of the position of the flapping/pitching wing with respect to the off-set angle γ_1. With y the distance from the axis of rotation,

$$h(y,t) = y\sin\left(\gamma_1 + \gamma_0\sin\frac{2\pi t}{T}\right) = h_1(y) + h_0(y)\sin\left(\frac{2\pi t}{T}\right) \approx |y|\gamma_1 + |y|\gamma_0\sin\frac{2\pi t}{T}, \tag{5}$$

so that $h_1(y) = |y|\gamma_1$ and $h_0(y) = |y|\gamma_0$. It then follows:

$$\frac{\partial h(y,t)}{\partial t} = |y|\gamma_0 2\pi f \cos\frac{2\pi t}{T}. \tag{6}$$

Substitution in the expression for the effective angle of attack, given in Eq. (4), yields

$$\alpha_{eff}(y,t) = [\theta_1 + \theta_0 \sin\left(\frac{2\pi t}{T} + \phi\right)] - \arctan\left(\pi \frac{f2|y|\gamma_0}{U_\infty} \cos\frac{2\pi t}{T}\right) \text{ for } y \in [-b/2, b/2]. \tag{7}$$

Note that the angle of attack of the configuration is included in the effective angle of attack α_{eff}.

In terms of dimensionless quantities, the effective angle of attack of a wing section becomes:

$$\alpha_{eff}\left(\frac{y}{b/2}, \frac{t}{T}\right) = [\theta_1 + \theta_0 \sin\left(2\pi\frac{t}{T} + \phi\right)] - \arctan\left(\pi St \frac{|y|}{b/2} \cos 2\pi\frac{t}{T}\right), \tag{8a}$$

with the Strouhal number defined as

$$St \equiv \frac{f2h_0(b/2)}{U_\infty}, \tag{8b}$$

in terms of the distance $2h_0(b/2) = b\gamma_0$ covered by the wing tip during one period of the motion. Eq. (8) shows that the effective angle of attack depends on four independent parameters, i.e.,

$$\alpha_{eff} = \alpha_{eff}\left(\frac{y}{b/2}, \frac{t}{T}; \theta_1, \theta_0, \phi, St\right). \tag{9}$$

Figure 4, left plot, presents for a representative set of parameters the effective angle of attack, during one cycle, at the tip of the wing $\frac{y}{b/2} = \pm 1$. The right plot of Fig. 4 illustrates the spanwise distribution of the effective angle of attack along the span of the wing.
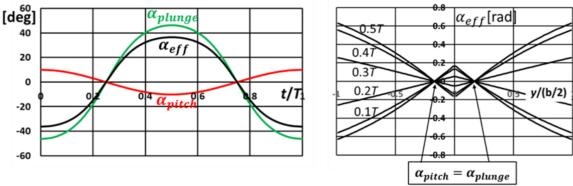

Figure 4 – Effective angle of attack $\alpha_{eff}(y/0.5b, t/T)$ due to plunging/pitching motion. Left: as function of t/T at wing tips y/(b/2)= $\pm$1. Right: as function of $y/(b/2)$ at six moments during half a cycle, from upstroke $t/T \in$ [0.0.25] to downstroke $t/T \in$ [0.25,0.5]. $\theta_1 = 0, \theta_0 = 10$ deg, $\phi = 90$ deg, St = 0.3343.

The left plot in Fig. 4 shows that the pitching motion, 90 deg out of phase with the plunging motion, reduces the amplitude of the angle of attack due to the plunge. It shows that at the wing tips the effect of the plunge dominates α_{eff}, however, the reduction of α_{eff} by the pitch mitigates the danger of flow separation. Note that, for this set of kinematic parameters, along the whole span, the plunge angle as well as the pitch angle and therefore the effective angle of attack, equal zero at t/T = 0.25 and 0.75 in the cycle, see also right plot in Fig. 4.

The derivative of $\alpha_{eff}\left(\frac{y}{b/2}, \frac{t}{T}\right)$ with respect to t/T follows from Eq. (8) as:

$$\frac{\partial}{\partial t}\alpha_{eff}\left(\frac{y}{b/2}, \frac{t}{T}\right) = 2\pi[\theta_0 \cos\left(2\pi\frac{t}{T} + \phi\right) + \frac{\pi St\frac{|y|}{b/2}\sin 2\pi\frac{t}{T}}{1 + \left(\pi St\frac{|y|}{b/2}\cos 2\pi\frac{t}{T}\right)^2}]. \tag{10}$$

For the case of ϕ = 90 deg, it follows that the derivative equals zero for t/T = 0, 0.5 and 1. The effective angle of attack at the start of the cycle and at the end of the cycle follow as

$$\alpha_{eff}\left(\frac{y}{b/2}, \frac{t}{T}\right) = \theta_1 + \theta_0 - \arctan\left(\pi St\frac{|y|}{b/2}\right), \text{ at } t/T = 0 \text{ and } 1, \text{ while} \tag{11}$$

$$\alpha_{eff}\left(\frac{y}{b/2}, \frac{t}{T}\right) = \theta_1 - \theta_0 + \arctan\left(\pi St\frac{|y|}{b/2}\right), \text{ at } t/T = 0.5. \tag{12}$$

Therefore, for the present case, at the wing tips, the minimum value of the effective angle of attack $\alpha_{eff,min} = -36.4$ deg at t/T = 0 and 1, while the maximum value equals $\alpha_{eff,max} = 36.4$ deg at t/T = 0.5. The rather high value of 36.4 deg for the instantaneous effective angle of attack at the wing tips is subject to uncertainties in the measured position of the tips of the (slightly flexible) wing of the wind-tunnel model. For higher values of θ_0, these maximum and minimum values of α_{eff} decrease in magnitude.

The right plot of Fig. 4 presents the distribution of the effective angle of attack $\alpha_{eff}\left(y/\frac{1}{2}b, t/T\right)$ as function of the spanwise coordinate, at six instants in time during half a flapping cycle. Since the angle of attack due to plunging decreases with decreasing y, the effect due to pitch and that due to plunge cancel at a certain value of y: here $\alpha_{eff} = 0$ at $y/\frac{1}{2}b \approx 0.17$, at all times. Subsequently, in the central part of the wing, $\alpha_{eff} = \alpha_{pitch} + \alpha_{plunge}$, changes sign, as is the loading of the inboard sections: the effect of pitching dominates the effective angle of attack. So, for the first half of the flapping cycle, about 1/6-th of the span of the wing features a decreasing α_{eff}, while both outboard panels experience an increasing α_{eff}. For the second half of the cycle this is the other way around. The expression for $\alpha_{eff}\left(\frac{y}{b/2}, \frac{t}{T}\right)$, Eq. (8), shows that, to first approximation, the effective angle of attack is close to linear in the spanwise coordinate $\frac{|y|}{b/2}$. This is confirmed in the right plot in Fig. 4,

3. Computational Method

3.1 Governing Equations

In the present study, it is assumed that the flow is incompressible, unsteady, inviscid and irrotational. The latter implies that the vorticity $\vec{\omega} \equiv \vec{\nabla} \times \vec{u} = \vec{0}$, leading to the introduction of the velocity potential $\Phi(x, y, z, t)$, such that $\vec{u}(x, y, z, t) \equiv \vec{\nabla}\Phi(x, y, z, t)$, which satisfies the irrotationality condition implicitly. For incompressible flow the continuity equation reduces to the condition that the flow is divergence-free: $\vec{\nabla}.\vec{u} = 0$. Therefore $\nabla^2\Phi = 0$, i.e., the velocity potential $\Phi(x, y, z, t)$ satisfies Laplace's equation:

$$\frac{\partial^2 \Phi}{\partial x^2} + \frac{\partial^2 \Phi}{\partial y^2} + \frac{\partial^2 \Phi}{\partial z^2} = 0. \tag{13}$$

In the present case the wing is slender (high-aspect ratio AR), thin and mildly cambered. Therefore, the wing is modelled as an infinitesimally-thin flat lifting surface S_{wi}, like sketched in Fig. 5 (left). The wake is attached to the trailing edge (TE) as the time-dependent wavy surface S_{wa}. For small-amplitude motion the lifting surface and its time-dependent wake are projected on the plane $z = 0$, where linearized boundary conditions are imposed, e.g., [22]. The wing reference surface $S_{wi} + S_{wa}$, i.e., $x \in [0, c], y \in [-b/2, b/2]$ carries a dipole distribution $\mu(x, y, t)$ with the edge conditions $\mu(x = 0, y, t) = 0$ and $\mu(x, \pm b/2, t) = 0$. The wake reference surface $x \in [c, \infty], y \in [-b/2, b/2]$ also carries a dipole distribution $\mu(x, y, t)$ with the edge condition $\mu(x, \pm b/2, t) = 0$ and along the connection between wing and wake the continuity condition $\mu(c^-, y, t) =$ and $\mu(c^+, y, t)$. Along the edge far downstream $\mu(x = \infty, y, t) \neq 0$ except for $y = \pm b/2$, which corresponds to the vortex filament that formed at the very start of the motion of the wing, a very long time ago.

The dipole distribution $\mu(x, y, t)$, a scalar quantity, is equivalent to a vortex distribution $\vec{\gamma}(x, y, t)$, a surface-vector quantity, through the relation:

$$\vec{\gamma}(x, y, t) = \vec{e}_n \times \vec{\nabla}\mu, \tag{14}$$

Eq. (14) implies that the surface vector $\vec{\gamma}$ is tangential to the plane $z = 0$ and is simultaneously normal to the gradient $\vec{\nabla}\mu$ of the dipole distribution. The vector $\vec{\nabla}\mu$ is a surface vector perpendicular to the iso-contours of the dipole strength. Vortex lines, similar to streamlines, are defined as curves everywhere tangential to $\vec{\gamma}$. Therefore, it follows from Eq. (14) that vortex lines coincide with iso-dipole contours on the plane $z = 0$. So, conveniently, an iso-dipole plot on the surface is equivalent to a plot of vortex lines on the plane $z = 0$.

A discontinuity in the dipole distribution corresponds to a vortex filament along the curve along which the dipole strength is discontinuous, with the strength of the vortex filament equal to the local value of the discontinuity in the dipole distribution.

The formulation in terms of the dipole distribution intrinsically obeys Kelvin-Helmholtz's vortex laws. Specifically, any vortex line on $S(x, y, t)$ is either a closed curve in itself, or a curve on $S(x, y, t)$ that merges into a vortex filament and subsequently emerges from the vortex filament, in that way forming a closed vortex line.
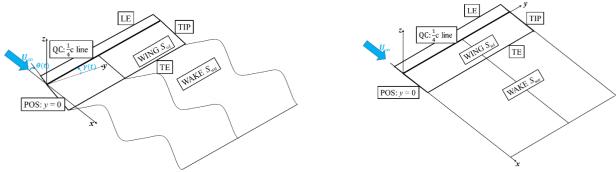
Figure 5 – Starboard side flapping-wing configuration at certain moment in cycle. Left: Flapping-pitching thin wing with wavy wake. Right: Stationary reference surface for application unsteady transpiration boundary conditions on wing and wake. Note that origin is on QC.

The velocity potential $\Phi(\vec{x}, t)$, at time t at point $\vec{x}$, is split in the contribution $U_\infty x$ due to the uniform free stream and a (perturbation) velocity potential $\varphi_d(\vec{x}, t)$ due to the dipole distribution on $S_{wi} + S_{wa}$, i.e.,

$$\Phi(\vec{x}, t) = U_\infty x + \varphi_d(\vec{x}, t), \text{ with } \varphi_d(|\vec{x}| \to \infty, t) \to 0. \tag{15}$$

The velocity potential $\varphi_d(\vec{x}_0, t)$ induced at $\vec{x}_0$, at time t, by the dipole distribution $\mu(\vec{x}, t)$, on the surface $S_{wi} + S_{wa}$, equals the surface integral:

$$\varphi_d(\vec{x}_0, t) = \frac{1}{4\pi} \iint_{S_{wi}+S_{wa}} \mu(\vec{x}, t) \frac{\vec{e}_n \cdot (\vec{x}_0 - \vec{x})}{|\vec{x}_0 - \vec{x}|^3} dS(\vec{x}), \tag{16}$$

with $\vec{x} = x\vec{e}_x + y\vec{e}_y$. In Eq. (16) $\vec{e}_n = \vec{e}_z$ is the unit vector perpendicular to the surface $S_{wi} + S_{wa}$, i.e., the plane $z = 0$, $\mu(\vec{x}, t) = \mu(x, y, t)$ and $dS(\vec{x}) = dxdy$.

The velocity $\vec{u}_d(\vec{x}_0, t) = \vec{\nabla}\varphi_d(\vec{x}_0, t)$ induced by the dipole distribution $\mu(x, y, t)$ on $S_{wi} + S_{wa}$ follows from taking the derivative of Eq. (16) with respect to $\vec{x}_0$. The derivation of obtaining $\vec{\nabla}\varphi_d(\vec{x}_0, t)$ is given amongst others in Ref. 22. It yields:

$$\vec{u}_d(\vec{x}_0, t) = \frac{1}{4\pi} \iint_{S_{wi}+S_{wa}} \frac{\vec{\gamma}(x,y,t) \times (\vec{x}_0 - \vec{x})}{|\vec{x}_0 - \vec{x}|^3} dxdy - \frac{1}{4\pi} \int_{\partial(S_{wi}+S_{wa})} \mu(x, y, t) \frac{(\vec{x}_0 - \vec{x}) \times \vec{dl}(\vec{x})}{|\vec{x}_0 - \vec{x}|^3}, \tag{17}$$

with, in the first term $\vec{\gamma}(x, y, t) = \vec{e}_z \times \vec{\nabla}\mu$, given in Eq. (14), the vortex distribution on the surface carrying the dipole distribution $\mu(x, y, t)$. The reference surface representing the wing and its wake, i.e., $S_{wi} + S_{wa}$, form a vortex sheet in 3D space.

The second term in Eq. (17) is recognised as the law of Biot and Savart for the velocity induced by a vortex filament in 3D space. In this case the vortex filament is along the boundary (i.e., the closed edge $\partial(S_{wi} + S_{wa})$ of the reference surface of the wing and its wake. The strength of the vortex filament equals the local strength $\mu(\vec{x} \in \partial(S_{wi} + S_{wa}), t)$ of the dipole distribution, while $\vec{dl}(\vec{x})$ is an infinitesimal element of the vortex filament running along its edge.

The surface integrals in Eqs. (16) and (17) are singular integrals, i.e., when $\vec{x}_0 \to \vec{x} = x\vec{e}_x + y\vec{e}_y$, a point on the dipole/vortex sheet, the integrands of the surface integrals tend to infinity. However, the result of the evaluation of these integrals, i.e., the velocity potential and the velocity, is finite, though discontinuous. To obtain this result, the integrals are evaluated as Cauchy-Principle-Value (CPV) integrals [22].

For $\vec{x}_0 \in \partial(S_{wi} + S_{wa})$, the second term in Eq. (17) for the induced velocity due to the vortex filament, is singular, like $1/r$, with r the distance from the filament. For a curved vortex filament there is an additional singular term that behaves like $\ln r$. In the present investigation both these terms are omitted from the induced velocity, or rather avoided by limiting the distance to the filament to a certain cut-off value.

The result for the velocity potential, of this CPV procedure, is that for $\vec{x}_0 \in S_{wi+wa}(x, y)$:

$$\varphi_d(\vec{x}_0, t) = \pm\frac{1}{2}\mu(x_0, y_0, t) + \frac{1}{4\pi}\text{CPV} \iint_{S_{wi}+S_{wa}} \mu(x, y, t) \frac{\vec{e}_z \cdot (\vec{x}_0 - \vec{x})}{|\vec{x}_0 - \vec{x}|^3} dxdy \tag{18}$$

and for the induced velocity:

$$\vec{u}_d(\vec{x}_0, t) = \pm\frac{1}{2}\vec{\gamma}(x_0, y_0, t) \times \vec{e}_z + \frac{1}{4\pi}\text{CPV} \iint_{S_{wi}+S_{wa}} \frac{\vec{\gamma}(x,y,t) \times (\vec{x}_0 - \vec{x})}{|\vec{x}_0 - \vec{x}|^3} dxdy - \frac{1}{4\pi}\int_{\partial(S_{wi}+S_{wa})} \mu(x, y, t) \frac{(\vec{x}_0 - \vec{x}) \times \vec{dl}(\vec{x})}{|\vec{x}_0 - \vec{x}|^3}, \tag{19}$$

with $\vec{\gamma} \times \vec{e}_z = \vec{\nabla}\mu = \frac{\partial\mu}{\partial x}\vec{e}_x + \frac{\partial\mu}{\partial y}\vec{e}_y$. In Eqs. (18) and (19) the $\pm$ symbol indicates that the quantity is positive on the upper side of $S_{wi+wa}(x, y)$ and negative on the lower side of $S_{wi+wa}(x, y)$.

3.2 Bernoulli's Equation

The momentum equation for irrotational, incompressible, inviscid flow, not subjected to a body force field, like gravity, reads:

$$\frac{\partial \vec{u}}{\partial t} + \vec{\nabla}\tfrac{1}{2}|\vec{u}|^2 + \vec{\nabla}\frac{p}{\rho_\infty} = \vec{0}. \tag{20}$$

Employing $\vec{u} = \vec{\nabla}\Phi$, then results, upon integration with respect to space, in Bernoulli's equation for incompressible, irrotational, inviscid flow not subjected to body forces, i.e.,

$$\frac{\partial \Phi}{\partial t} + \tfrac{1}{2}\left|\vec{\nabla}\Phi\right|^2 + \frac{p}{\rho_\infty} = C(t), \tag{21}$$

with $C(t)$ independent of position in space, so, either a constant, or the same function of time in the whole space. In the present case, the constant is evaluated in the far- field, which yields $C(t) = C = \frac{1}{2}U_\infty^2 + \frac{p_\infty}{\rho_\infty}$, so that with $\Phi(\vec{x}, t) = U_\infty x + \varphi_d(\vec{x}, t)$ and $\vec{\nabla}\Phi(\vec{x}, t) = U_\infty \vec{e}_x + \vec{u}_d(\vec{x}, t)$ and with the pressure coefficient $C_p(\vec{x}, t)$ defined as $C_p(\vec{x}, t) \equiv \frac{p(\vec{x}, t) - p_\infty}{\frac{1}{2}\rho_\infty U_\infty^2}$, $\tag{22}$

$$C_p(\vec{x}, t) = -\frac{2}{U_\infty^2}\frac{\partial \varphi_d}{\partial t} - [2\frac{\vec{e}_x \cdot \vec{u}_d}{U_\infty} + \frac{|\vec{u}_d|^2}{U_\infty^2}]. \tag{23}$$

For points on the wing and on the wake in the plane $z = 0$, it follows

$$C_p(x, y, t) = -\frac{2}{U_\infty^2}\frac{\partial \varphi_d}{\partial t} - \frac{2}{U_\infty}u_d(x, y, t) - \frac{2}{U_\infty^2}|\vec{u}_d(x, y, t)|^2. \tag{24}$$

In this expression, the first two terms are linear, while the third term is quadratic, which is neglected in the linearized formulation.

3.3 Boundary Conditions

In order to solve for the dipole distribution on the wing S_{wi}, the boundary condition is the normal-velocity condition, i.e., the no-penetration condition

$$(\vec{u} - \vec{u}_{wi}).\vec{e}_n = 0, \text{ for points on } S_{wi}, \tag{25}$$

which assures that, in normal direction, the wing surface moves at the same speed as the flow. In order to impose this condition, it has to be converted into a transpiration condition to be applied at the reference surface. In the present study, in which a lifting-line method has been developed, this is not needed.

On the wake surface S_{wa}, both the dipole distribution and the wake surface are to be solved for. Therefore, two boundary conditions have to be imposed: the normal-velocity boundary condition, Eq. (25) and the condition that the wake surface does not carry a load, i.e., that the pressure difference across the wake surface equals zero. Equation (24) applied at S_{wa}, yields:

$$\Delta C_p(x, y, t) = -\frac{2}{U_\infty^2}\frac{\partial \Delta \varphi_d}{\partial t} - \frac{2}{U_\infty}\Delta u_d(x, y, t) - \frac{2}{U_\infty^2}\Delta[|\vec{u}_d(x, y, t)|^2], \text{ for points on } S_{wa}. \tag{26}$$

3.4 Prandtl's Lifting-Line Theory

The lifting-line theory of Prandtl for high-aspect-ratio wings in **steady**, incompressible, irrotational (potential) flow, can be phrased in terms of the dipole/vortex-distribution formulation described in section 3.1, see Fig. 5 (right). From Eq. (14) it follows that, on the reference surface $z = 0$ of the wing and its wake, the vortex distribution $\vec{\gamma}(x, y)$ can be expressed in terms of the partial derivatives of the dipole distribution $\mu(x, y)$ as:

$$\vec{\gamma}(x, y) = \vec{e}_z \times \vec{\nabla}\mu = -\frac{\partial \mu}{\partial y}\vec{e}_x + \frac{\partial \mu}{\partial x}\vec{e}_y. \tag{27}$$

The spanwise component $\gamma_y(x, y)$ of the wing vortex distribution is lumped into the circulation $\Gamma_{c/4}(y)$ of the wing, through

$$\Gamma_{c/4}(y) \equiv \int_0^c \gamma_y(x, y)dx = \int_0^c \frac{\partial \mu}{\partial x}dx = \mu(c, y),), \text{ for } y \in [-b/2, b/2], \tag{28}$$

where the (leading-)edge condition $\mu(0, y) = 0$ has been imposed. For each section $y = $ constant of the wing, the circulation $\Gamma_{c/4}(y)$ is positioned at the center-of-vorticity (COV) of the vortex distribution $\gamma_y(x, y)$, with

$$x_{COV}(y)\Gamma_{c/4}(y) \equiv \int_0^c x\gamma_y(x, y)dx. \tag{29}$$

Prandtl placed the circulation at the ¼-chord line of the wing. This can be related to the classical complex-function solution of the incompressible 2D potential flow about a flat plate at angle of attack, e.g. [25]. Alternatively, it can be related to Prandtl's thin-airfoil solution for incompressible 2D

potential flow about a flat plate at angle of attack, e.g. [26]. From this solution it follows $\gamma_y(x) = A\sqrt{(c-x)/x}$, with constant A proportional to the free stream velocity U_∞ and the angle of attack.
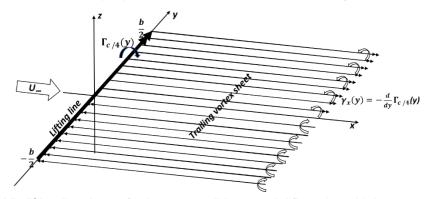

Figure 6 – Prandtl's lifting-line theory for incompressible potential flow about high-aspect ratio wing at angle of attack. Note that origin coordinate system is on lifting line.

Substitution of this solution in Eq. (29) leads to $x_{COV} = c/4$. The dipole distribution on the wing and wake in Fig. 5 (right) is now, see Fig. 6

$$\mu(x,y) = \Gamma_{c/4}(y), \text{ for } x \in [0,\infty) \text{ and } y \in [-b/2, b/2], \tag{30}$$

equivalent to a spanwise vortex filament of strength $\Gamma_{\frac{c}{4}}(y)$, with $\Gamma_{c/4}(\pm b/2) = 0$, and a continuous distribution of the chordwise component $\gamma_x(y) = -\dfrac{d}{dy}\Gamma_{c/4}(y)$ of the vortex distribution on the region downstream of the lifting line. Finally, formally, there is also a vortex filament of strength $-\Gamma_{c/4}(y)$ along the line $x = \infty$, $z = 0$, for $y \in [-b/2, b/2]$, the so-called start vortex, but its induced velocity at the lifting line is infinitesimally small. Note that a vortex line starting in the lifting-line running in spanwise direction, emerges at some point along the span, turns abruptly in chordwise direction, continues straight on until at infinity downstream it meets the start vortex filament. There it turns abruptly in negative *y*-direction and runs chordwise upstream, until it meets the lifting-line vortex filament, where it turns abruptly in positive *y*-direction until it arrives at its initial point, completing the closed circuit, obeying the Kelvin-Helmholtz vortex laws.

In Prandtl's lifting-line method the distribution of the circulation $\Gamma_{c/4}(y)$ along the lifting line is obtained from an integro-differential equation that evolves from an intricate combination of the relation for sectional lift $\ell(y)$ [N/m], obtained from the Kutta-Joukowski Theorem for the force on a vortex filament and the expression for the sectional lift in terms of the slope $a_0 = 2\pi$ of the sectional lift vs angle-of-attack curve, obtained from thin-airfoil theory.

The Kutta-Joukowski Theorem, provides the sectional lift $\ell(y)$ in terms of the circulation $\Gamma_{c/4}(y)$ of the wing, the free-stream velocity U_∞ and the density ρ_∞, as

$$\ell(y) = \rho_\infty U_\infty \Gamma_{c/4}(y). \tag{31}$$

Thin-airfoil theory gives the lift coefficient $c_\ell(y)$ in terms of the slope $\dfrac{d}{d\alpha}c_\ell(y) = a_0(y)$ of the lift curve $c_\ell(\alpha)$, the dynamic pressure $q_\infty = \frac{1}{2}\rho_\infty U_\infty^2$, the chord $c(y)$ of the airfoil section and the effective angle of attack of the airfoil section:

$$\ell(y) \equiv \tfrac{1}{2}\rho_\infty U_\infty^2 c_\ell(y)c(y), \tag{32}$$

with the lift coefficient $c_\ell(y)$ expressed as

$$c_\ell(y) = a_0(y)(\alpha - \alpha_0(y) + \beta(y) + \tfrac{w_{in}(y)}{U_\infty}), \tag{33}$$

with α the geometric angle of attack of the wing, $\alpha_0(y)$ the zero-lift angle of attack of the airfoil sections making up the wing, $\beta(y)$ the spanwise distribution of the twist angle of the wing, with at the root of the wing $\beta(0) = 0$ and finally, $w_{in}(y)$ the *z*-component of the velocity induced at the lifting line by the trailing vortex sheet. Combining Eqs. (31)-(33) yields

$$\Gamma_{\frac{c}{4}}(y) = \tfrac{1}{2}U_\infty c(y)a_0(y)[\alpha - \alpha_0(y) + \beta(y) + \tfrac{w_{in}(y)}{U_\infty}], \text{ for } y \in [-b/2, b/2] \tag{34}$$

The upwash $w_{in}(y)$, induced by the vortex distribution $\gamma_x(y) = -\dfrac{d}{dy}\Gamma_{c/4}(y)$ on the trailing vortex sheet, $(x \in [0,\infty), y \in [-b/2, b/2], z = 0)$, see Fig. 6, follows from Eq. (19) as

8

$$w_d(x_0, y_0, z_0 = 0) = \frac{1}{4\pi} \text{CPV} \int_{-b/2}^{b/2} \left[-(y_0 - y) \frac{d}{dy} \Gamma_{c/4}(y) \int_0^\infty \frac{dx}{[(x_0-x)^2 + (y_0-y)^2]^{3/2}} \right] dy$$

The integral with respect to *x* can be evaluated analytically, which leads to

$$w_d(x_0, y_0, z_0 = 0) = \frac{-1}{4\pi} \text{CPV} \int_{-b/2}^{b/2} \frac{1}{y_0 - y} \frac{d}{dy} \Gamma_{c/4}(y) \left[1 + \frac{x_0}{[x_0^2 + (y_0-y)^2]^{1/2}} \right] dy.$$

The upwash to be substituted in Eq. (34) equals $w_{in}(y_0) = w_d(x_0 = 0, y_0, z_0 = 0)$, so that

$$w_{in}(y) = \frac{-1}{4\pi} \text{CPV} \int_{-b/2}^{b/2} \frac{1}{y-\eta} \frac{d}{d\eta} \Gamma_{c/4}(\eta) d\eta.$$

Substitution in Eq. (34) yields the integro-differential equation for $\Gamma_{c/4}(y)$:

$$\Gamma_{c/4}(y) = \frac{1}{2} U_\infty c(y) a_0(y) [\alpha - \alpha_0(y) + \beta(y) - \frac{1}{4\pi U_\infty} \text{CPV} \int_{-\frac{b}{2}}^{\frac{b}{2}} \frac{1}{y-\eta} \frac{d}{d\eta} \Gamma_{c/4}(\eta) d\eta], \text{ for } y \in [-b/2, b/2]. \quad (35)$$

3.5 Kutta-Joukowski Theorem for Unsteady Flow

The flow about a flapping wing is an unsteady flow problem. In the case of **unsteady**, incompressible, potential flow, Laplace's equation, Eq. (13), is the governing equation for the velocity potential, like for steady, incompressible, potential flow. The unsteadiness enters the problem through the boundary conditions, i.e., the motion of the wing. Furthermore, as a consequence of the temporal variation of the circulation, the wake is now a vortex sheet of strength depending on the history of the circulation of the wing, i.e., of the history of the motion of the wing.

For unsteady flow, Eq. (31) has to be adjusted since the classical Kutta-Joukowski Theorem is for steady flow only. For unsteady potential flow, Eq (24) for the pressure coefficient $C_p(x, y, t)$ has been derived from the momentum equation for unsteady, incompressible potential flow. From Eq. (24) the pressure jump across the wing reference surface S_{wi} is derived, to first order in the perturbations, as:

$$\Delta C_p(x, y, t) \equiv \frac{p(x,y,z=0^-) - p(x,y,z=0^+)}{\frac{1}{2}\rho_\infty U_\infty^2} = \frac{2}{U_\infty} \left[\frac{\partial \Delta \varphi}{\partial x} + \frac{1}{U_\infty} \frac{\partial \Delta \varphi}{\partial t} \right] + h.o.t., \text{ with} \quad (36)$$

$\varphi(x, y, z, t)$ the perturbation velocity potential and $\Delta\varphi \equiv \varphi(x, y, z = 0^+) - \varphi(x, y, z = 0^-)$. In the present formulation the reference wing, as well as the wake, carry a dipole distribution $\mu(x, y, t)$, so that the jump in the perturbation potential can be expressed as $\Delta\varphi(x, y, 0, t) = \mu(x, y, 0, t)$. Then Eq. (36) becomes

$$\Delta C_p(x, y, 0, t) = \frac{2}{U_\infty} \left[\frac{\partial \mu}{\partial x} + \frac{1}{U_\infty} \frac{\partial \mu}{\partial t} \right] \quad (37)$$

To derive an expression for the Kutta-Joukowski Theorem for unsteady flow about thin wings, the pressure difference given in Eq. (37) is integrated along the section of the wing reference surface, situated in the plane *z* = 0, i.e.,

$$\frac{\ell(y,t)}{\frac{1}{2}\rho_\infty U_\infty^2 c(y)} = \frac{2}{c(y)} \int_0^{c(y)} \Delta C_p(x, y, t) dx = \frac{2}{c(y) U_\infty} \int_0^{c(y)} \left[\frac{\partial \mu}{\partial x} + \frac{1}{U_\infty} \frac{\partial \mu}{\partial t} \right] dx. \quad (38)$$

Since, $\int_0^{c(y)} \frac{\partial \mu}{\partial x}(x, y, t) dx = \mu(c(y), y, t) = \Gamma_{c/4}(y, t)$, it follows:

$$\frac{\ell(y,t)}{\frac{1}{2}\rho_\infty U_\infty^2 c(y)} = \frac{2}{c(y) U_\infty} \left[\Gamma_{c/4}(y, t) + \frac{1}{U_\infty} \frac{\partial}{\partial t} \int_0^{c(y)} \mu(x, y, t) dx \right] \quad (39)$$

Consider the integral in Eq. (39). Partial integration gives, with $\frac{\partial \mu}{\partial x} = \gamma_y$:

$$\int_0^{c(y)} \mu(x, y, t) dx = [\mu(x, y, t) x]_0^{c(y)} - \int_0^{c(y)} x \frac{\partial}{\partial x} \mu(x, y, t) dx = \Gamma_{c/4}(y, t) c(y) - \int_0^{c(y)} x \gamma_y(x, y, t) dx.$$

Therefore, with the definition of the center-of-gravity of the spanwise component of the vortex distribution defined in Eq. (29), Eq. (39) results in

$$\frac{\ell(y,t)}{\frac{1}{2}\rho_\infty U_\infty^2 c(y)} = \frac{2}{c(y) U_\infty} \left[\Gamma_{c/4}(y, t) + \frac{1}{U_\infty} \frac{\partial}{\partial t} \left\{ \Gamma_{c/4}(y, t) c(y) \left\{ 1 - \frac{x_{cov}(y,t)}{c(y)} \right\} \right\} \right] \quad (40)$$

Similar to the argumentation following Eq. (29), it is assumed that $\frac{x_{cov}(y,t)}{c(y)} \approx \frac{1}{4}$. Then it follows

$$\frac{\ell(y,t)}{\frac{1}{2}\rho_\infty U_\infty^2 c(y)} = \frac{2}{c(y) U_\infty} \left[\Gamma_{c/4}(y, t) + \frac{3}{4} \frac{c(y)}{U_\infty} \frac{\partial}{\partial t} \Gamma_{c/4}(y, t) \right],$$

so that the Kutta-Joukowski Theorem for unsteady flow reads:

$$l(y, t) = \rho_\infty U_\infty \left[\Gamma_{c/4}(y, t) + \frac{3}{4} \frac{c(y)}{U_\infty} \frac{\partial}{\partial t} \Gamma_{c/4}(y, t) \right]. \quad (41)$$

The relation presented in Eq. (41) is different from the relation for the section lift coefficient as for example given in [27], which instead of the factor $\frac{3}{4}$ features the factor 1.0 in the added=-mass contribution to the section lift.

3.6 Lifting-Line Theory for Unsteady Flow

For the case of steady flow, the lifting-line integro-differential equation follows from the combination of Eqs. (31), (32) and (33). For unsteady flow Eq. (31), the classical Kutta-Joukowski Theorem, is replaced by its unsteady version. Then Eq. (34) becomes

$$\Gamma_{c/4}(y,t) + \frac{3}{4}\frac{c(y)}{U_\infty}\frac{\partial}{\partial t}\Gamma_{c/4}(y,t) = \frac{1}{2}U_\infty c(y)a_0(y)[\alpha_{eff}(y,t) - \alpha_0(y) + \beta(y) + \frac{w_{in}(y,t)}{U_\infty}],$$

for $y \in [-b/2, b/2]$ and $t > 0$. (42)

In Eq. (42) the upwash $w_{in}(y,t)$ due to the dipole distribution on the wing between lifting line at $x = c(y)/4$ and the trailing edge and the dipole distribution on the wake, which runs from $x = x_{TE} = c(y)$ to infinity downstream, see Fig. 5-right, equals

$$w_{in}(y,t) = \frac{1}{4\pi}\int_{-\frac{b}{2}}^{\frac{b}{2}}d\eta[\int_{c(y)/4}^{c(y)}\frac{(y-\eta)\gamma_x(\eta,t)}{[x^2+(y-\eta)^2]^{\frac{3}{2}}}dx + \int_{c(y)}^{\infty}\frac{(y-\eta)\gamma_x(x,\eta,t)+x\gamma_y(x,\eta,t)}{[x^2+(y-\eta)^2]^{\frac{3}{2}}}dx], \text{ for } y \in [-b/2, b/2]. \quad (43)$$

Note that between the lifting line at $x = c/4$ and the trailing edge at $x = c$, the wing reference surface carries a dipole distribution $\mu(x,y,t) = \Gamma_{c/4}(y,t)$, which corresponds to a vortex distribution $\gamma_x(y,t)$ with a chordwise component only.

Equation (43) is an integro-differential equation for $\Gamma_{c/4}(y,t)$. However, now the situation is more complicated than for the case of steady flow in that the strength (circulation) $\Gamma_{c/4}(y,t)$ of the lifting line is time-dependent, while the wake carries a dipole distribution $\mu(x,y,t)$ that depends not only on y, but on x, y and t, so that both components of the vortex distribution, i.e., $\gamma_x = -\frac{\partial\mu}{\partial y}$ and $\gamma_y = \frac{\partial\mu}{\partial x}$ have to be considered.

3.7 Boundary Conditions on Wake

The wake is subject to two boundary conditions, see section 3.2. In the present study, the condition that the wake surface should be a stream surface, Eq. (25), is omitted since the true wake surface is not part of the formulation, i.e., just the wake reference surface $z = 0$ is considered. Note that once the dipole distribution has been determined, the planar wake reference surface features a distribution of non-zero normal velocity that might be used to update the geometry of the wake surface in an iterative manner.

The second condition, Eq. (26), that across the wake the jump in pressure ΔC_p equals zero, is employed to determine the spatial and temporal strength of the wake dipole distribution. Equation (37) applied to the wake reference surface reads:

$$\Delta C_p(x > x_{TE}, y, t) = \frac{2}{U_\infty}\left[\frac{\partial\mu}{\partial x} + \frac{1}{U_\infty}\frac{\partial\mu}{\partial t}\right] = 0, \text{ for } y \in [-b/2, b/2] \text{ and } t > 0. \quad (44)$$

Eq. (44) is recognized as a first-order wave equation in (x,t)-space, for $\mu(x,y,t)$ convecting with constant velocity U_∞ in x-direction. At time t the solution equals:

$$\mu(x,y,t) = \Gamma_{c/4}\left(y, t - \frac{x-x_{TE}}{U_\infty}\right), \text{ for } x \in [x_{TE}, x_{TE} + U_\infty t], y \in [-b/2, b/2] \text{ and } t > 0. \quad (45)$$

The classical Lifting-line method does not require a Kutta condition at the trailing edge: Actually, in the problem formulation there is not a solid part of the wing nor a trailing edge. For the unsteady-flow version of the lifting-line method there is a trailing edge, at $x = c$, which forms the connection between the wing and the wake. This implies that a Kutta condition is to be imposed on the solution. The condition that is imposed is that at the trailing edge, the pressure difference between upper and lower side of the surface equals zero at all times. This implies that the linearized equation given in Eq. (44) is not only applied on the wake surface, but also at the trailing edge. Therefore, the Kutta condition for unsteady flow reads:

$$\Delta C_p(x = x_{TE} = c, y, t) = \frac{2}{U_\infty}\left[\frac{\partial\mu}{\partial x} + \frac{1}{U_\infty}\frac{\partial\mu}{\partial t}\right] = 0, \text{ i.e., } \frac{\partial\mu}{\partial x} + \frac{1}{U_\infty}\frac{\partial\mu}{\partial t} = 0, \quad (46)$$

for $x = x_{TE} = c, z = 0$, along the span of the trailing edge, for all times.

3.8 Spanwise Lift and Drag Distributions

The spanwise distribution of section lift $\ell(y,t)$ is given in Eq. (41), repeated here, in terms of the unsteady Kutta-Joukowski Theorem.

$$l(y,t) = \rho_\infty U_\infty \left[\Gamma_{c/4}(y,t) + \frac{3}{4}\frac{c(y)}{U_\infty}\frac{\partial}{\partial t}\Gamma_{c/4}(y,t) \right]. \tag{41}$$

The section drag $d(y,t)$ follows from application of the Kutta-Joukowski Theorem to the lifting-line vortex filament subject to an upwash velocity component:

$$d(y,t) = -\rho_\infty U_\infty \left[\frac{w_{in}(y,t)}{U_\infty} - \frac{1}{U_\infty}\frac{\partial h(y,t)}{\partial t} \right] \Gamma_{c/4}(y,t) \tag{47}$$

The term inside the square brackets is the velocity in z-direction, relative to the flapping motion of the lifting line, consisting of the contribution induced by the dipole distribution on the wing and on the wake, with the upwash corrected for the time-derivative of the position of the lifting line. Once the circulation distribution of the lifting-line has been determined from the Unsteady-Lifting-Line integro-differential equation, Eq. (42), the velocity induced at the lifting line by the dipole distribution follows as

$$\frac{w_{in}(y,t)}{U_\infty} = \frac{2}{a_0(y)}\frac{\bar{c}}{c(y)}\frac{1}{U_\infty \bar{c}}\left[\Gamma_{c/4}(y,t) + \frac{3}{4}\frac{c(y)}{U_\infty}\frac{\partial}{\partial t}\Gamma_{c/4}(y,t) \right] - [\alpha_{eff}(y,t) - \alpha_0(y) + \beta(y)] \tag{48}$$

Equation (4) gives the effective angle $\alpha_{eff}(y,t)$ of attack as the sum of the pitch angle $\theta(t)$ and the plunge angle $-\frac{1}{U_\infty}\frac{\partial h(y,t)}{\partial t}$. Substitution in Eq. (47) yields:

$$d(y,t) = -\rho_\infty U_\infty \Gamma_{c/4}(y,t) \left[\frac{2}{a_0(y)}\frac{\bar{c}}{c(y)}\frac{1}{U_\infty \bar{c}}\left\{ \Gamma_{c/4}(y,t) + \frac{3}{4}\frac{c(y)}{U_\infty}\frac{\partial}{\partial t}\Gamma_{c/4}(y,t) \right\} - \{\theta(t) - \alpha_0(y) + \beta(y)\} \right] \tag{49}$$

The section lift coefficient $c_l(y,t)$ and section drag $c_d(y,t)$ coefficient then follow by dividing left- and right-hand side of Eqs. (41) and (49) by $\frac{1}{2}\rho_\infty U_\infty^2 c(y)$.

4   Application Lifting-Line Method for Unsteady Flow

4.1 Parameters of flapping wing motion

The present Unsteady Lifting-Line Method has been applied to simulate the flow about the flapping wing of the wind-tunnel model of the Robird at a free stream velocity of U_∞= 6 m/s, flapping frequency f = 3 Hz and spanwise uniform pitching with amplitude θ_0 = 0(2.5)20 deg, without off-set (θ_1= 0 deg), with phase angle ϕ = 90 deg. The amplitude of the flapping motion equals γ_0 = 34.2 deg, with offset γ_1 = 7.5 deg. All parameters of the flapping motion are listed in Table 1. Note that the Strouhal number St, defined in Eq. (8b) is a combination of flapping/pitching frequency f, free-stream velocity U_∞ and the amplitude $2h_0$ (which is proportional to γ_0) of the flapping motion at the wing tips. Dimension analysis shows that, using $(\rho_\infty, U_\infty, b)$, the dimensionless aerodynamic properties A of the flapping wing motion can be expressed as $A = A(St, \theta_0, \gamma_1, \theta_1, \phi, \alpha, AR)$. In the present study the focus is on the dependency of the aerodynamic properties on the amplitude of the pitching motion θ_0 and on the Strouhal number St.

Table 1 – Flapping wing parameters in application Unsteady-Lifting-Line Method.

γ_1	7.5 deg	U_∞	6 m/s	$2h_0(y/0.5b = \pm 1)$	0.67 m
γ_0	34.2 deg	f	3 Hz	St	0.3343
θ_1	0	α	0		
θ_0	0(2.5)20 deg				
ϕ	90 deg				

4.2 Geometry simplified wing

The spanwise distribution of the chord $c(y)$ of the Robird wing (Fig. 1) has been simplified to a piecewise linear distribution, symmetric with respect to the plane-of-symmetry y = 0. The half-span is subdivided in three parts:

$y \in [0.0, 0.182]$ m   : $c(y) = 0.2$ m
$y \in [0.182, 0.476]$ m: $c(y) = [0.200(0.476 - y) + 0.102(y - 0.182)]/0.294$ m
$y \in [0.476, 0.560]$ m: $c(y) = [0.102(0.560 - y) + 0.010(y - 0.476)]/0.084$ m
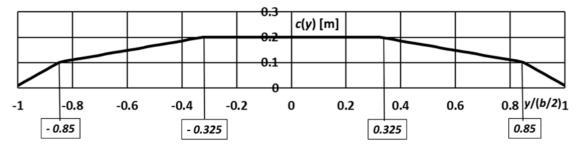The distribution is shown in Fig. 7.

Figure 7 - Spanwise distribution of chord $c(y/0.5b)$ of simplified planform of wind-tunnel model Robird.

Table 2 - Geometric parameters of simplified flapping-wing configuration.

b	1.12 m
c_0	0.2 m
$\bar{c}$	0.1527 m
AR	7.34

For reasons of convenience of modeling, the wing of the simplified configuration extends from the root of the wind-tunnel model to the plane of symmetry $y = 0$, i.e., the gap between the root of the wind-tunnel model and the fuselage of the configuration is closed and the wing span runs from the plane of symmetry to the wing tip.

For the wind-tunnel model the axis of rotation of the flapping motion is located at a distance of 0.04 m from the plane of symmetry of the configuration. For the simplified configuration the axis of rotation of the flapping motion of the wing is located in the plane of symmetry, i.e., along the x-axis.

4.3 Discretization flapping-wing configuration

For the purpose of application of the present Unsteady-Lifting-Line method to the simplified flapping-wing configuration, the linearized (transpiration type of) boundary conditions are imposed on a rectangular domain of span b and chord $\bar{c}$ in the plane $z = 0$, but, the effect of $c(y)$ is retained in the formulation. The free-stream velocity is parallel to this plane, directed in positive x-direction ($\alpha = 0$). The lifting line of the simplified flapping-wing configuration is located along the quarter-chord line ($x = 0, y \in [-b/2, b/2], z = 0$). The trailing edge (TE) is located at ($x = 3\bar{c}/4, y \in [-b/2, b/2], z = 0$). The lifting line is divided into $N = 80$ elements, here in a uniform distribution. The chord $c(y)$ of the airfoil sections and the effective angle of attack $\alpha_{eff}(y, t)$ are assigned to the mid-points (collocation points) of the N elements on the lifting line. The circulation $\Gamma_{c/4}(y, t)$ of the lifting line is discretised by element-wise quadratic representations $f(y)$ based on $\Gamma_{c/4}(y, t)$, at three consecutive collocation points: $y = y_{k-1}, y_k$ and y_{k+1}, with $\Gamma_{c/4}(y_k, t)$, for $k = 1(1)N$ as unknowns to be determined. The N unknown $\Gamma_{c/4}(y_k, t)$'s are solved for in the Unsteady Lifting-Line method. Across the edges of the elements, the element-wise quadratic representations $f(y)$ are continuous in function value and in first derivative, guaranteeing a continuous, second-order accurate representation of the dipole distribution $\mu(x, y, t)$ on wing and wake.
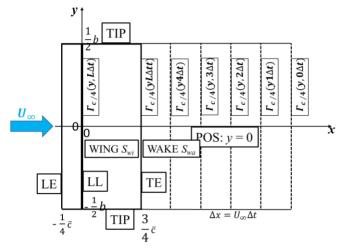

Figure 8 – Time-stepping procedure progressed to time $t = L\Delta t$, $L = 5$.

Figure 8 shows that between the lifting line at $x = 0$ and the TE at $x = 3\bar{c}/4$, the dipole distribution $\mu(x,y,t) = \Gamma_{c/4}(y,t)$, i.e., $\mu(x,y,t)$ is constant in x-direction, therefore, the discretization consists of a chord-wise strip conveying the circulation of the lifting line (LL) to the trailing edge (TE). The discretization of the wake, situated downstream of the TE, is tied to the time-stepping procedure used to obtain the time-dependent solution. For each new increment Δt in time, the trailing edge of the wake domain is extended by a spanwise strip of width $\Delta x = U_\infty \Delta t$. Then the dipole distribution on the wake is shifted in downstream direction, such that at time t: $\mu(x,y,t) = \mu(x - U_\infty \Delta t, y, t - \Delta t)$. The number of time steps per period t equals 20, i.e., $\frac{\Delta t}{T} = 0.05$. In the present study four full periods of the flapping motion have been simulated, i.e., the calculation comprises 80 time-steps.

5   Experimental Set-up

A model that represents the port-side of the Robird is placed in the open jet of the University of Twente (UT) Aeroacoustics wind tunnel, as shown in Fig. 9 [20]. In the model the full-size port-side wing of a Robird is mounted on a flapping mechanism. Three measurement volumes are defined at one chord-length downstream of the wing trailing edge, perpendicular to the incoming flow field. Each volume is considered in a separate measurement. The purpose of the present setup is to measure the velocity flow field in the wake of the Robird wing at a number of Strouhal numbers St for several pitching amplitudes θ_0. The goal of the measurement is twofold: (i) to confirm that a jet-like flow establishes during the flapping cycle, and (ii) to identify vortical structures traveling downstream in the wake.

Figure 9 - Full-scale Robird wing (black with checker pattern in root and tip region) mounted in open section of UT aeroacoustics wind tunnel. Also visible: calibration plate, blue articulated optic arm; two Phantom V611 high-speed cameras. Flow is from right to left.

5.1 Parameters Experiments

The parameters of the experiments are presented in Table 3. The Strouhal numbers St were: (i) St = 0.19, a value lower than the value for the Robird in cruising flight; (ii) St = 0.124, a value corresponding to the cruising flight condition and (iii) St = 0.31, the highest value achievable with the present setup. The values for the pitching amplitude θ_0 could not be chosen, as the flapping mechanism did not allow for independent variation of the pitching angle $\theta(t)$ nor of the flapping angle $\gamma(t)$. In a previous study [28], the flapping angle of an airfoil section at $y/0.5b = 0.45$ was studied.

Table 3 – Matrix of parameters experiments.

U_∞ [m/s]	f [Hz]	θ_0 at $y/0.5b = 0.45$ [deg]	St	Re
6	3	7.5	0.31	0.8×10^5
8	3	7	0.24	1.1×10^5
10	3	7	0.19	1.3×10^5

The pitching angle was found to mainly depend on flight velocity. The pitching angle amplitudes given in Table 3 are the values from this study. The Reynolds number is based on the mean chord of the wing.

5.2 Equipment and Procedure Experiments

Stereo-PIV measurements were performed to validate the results of the numerical method developed in the present study. Figure 10 shows a schematic top-view and side-view of the experimental setup. The measurement volume is imaged by two Phantom V611 cameras, each fitted with an AF Nikkor 60 mm *f*/2.8 D lens. Bandpass filters (532 nm) were fitted to each lens to reduce noise caused by reflections. The cameras have a resolution of 1200 pixels by 800 pixels. Lavision V4 Scheimpflug mounts were used to align the focal plane with the measurement plane. The cameras were positioned in a forward-scatter arrangement, with one camera on either side of the measurement volume. The opening angle *β* was approximately 50 deg. The measurement volume was illuminated with a Photonics Industries DM30 high-speed laser. The laser-light sheet thickness was approximately 5mm at the beam waist. The beam waist was aligned with the center of the measurement volume. The flow was seeded with liquid Di-Ethyl-Hexyl-Sulphate (DEHS) particles of approximately 1 μm in diameter. Measurements were performed at 600 Hz during 10 flapping cycles. Each measurement cycle was triggered by a trigger-pulse generated by the flapping device, which phase-locked the measurements. Initial calibration and perspective correction were carried out using a two-level calibration plate. Further errors were eliminated a posteriori with disparity mapping.

5.3 Data Acquisition and Processing

The data was processed with the DaVis 10.1 software package. Before processing, the calibration for each position (tip, middle and root) was corrected with a planar self-calibration routine that relies on disparity mapping. Prior to the PIV analysis, reflections were suppressed with a Gaussian time filter. The PIV analysis was performed with window shift and window deformation enabled. Two coarse passes with a window size of 48 pixels × 48 pixels were followed by a single fine pass with a window size of 24 pixels × 24 pixels. A spatial auto-mask was used to mask both the wing as well as poorly illuminated areas. The vector fields were post-processed with a universal outlier-detection algorithm [29]. Outliers were replaced with interpolated data. All datasets were phase-averaged over the 10 cycles measured. Finally, all measured flow structures are assumed to be convected with the flow, allowing the reconstruction of the wake shape in three-dimensional space. Vortical structures are assumed to be frozen in time, according to Taylor's frozen wake hypothesis. Although this hypothesis is demonstrably incorrect [17], on paper, it allows for the best representation of data acquired over time.
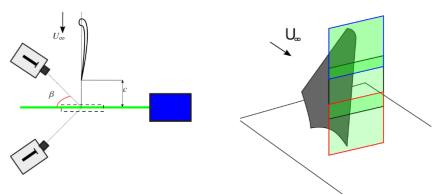

Figure - 10 Schematic of setup (a) top view: orientation of laser sheets, laser optics (blue box) and cameras (two grey objects at left side). (b) oblique view: three measurement volumes used, one at wing tip in blue, one at mid-wing section in black and one at root in red.

6 **Results**

6.1 Numerical Simulations

6.1.1 Wake Topology

Figure 11 presents iso-contours of the dipole distribution $\mu(x, y, t = 4T)/(U_\infty \bar{c})$ on the wing and on the wake of the simplified configuration at $t/T = 4$, i.e., after 4 periods of the flapping/pitching motion, with magnitude in pitching motion of $\theta_0 = 0(2.5)20$ deg. As reference, Fig. 11 includes, for every 5 deg increment in θ_0, the corresponding spanwise distributions of effective angle-of-attack during half an upstroke-downstroke cycle of the wing. The large bluish regions are formed during the upstroke ($t/T \in (0.75, 1.0/0.0, 0.25)$), while the larger reddish regions are formed during the downstroke ($t/T \in (0.25, 0.5, 0.75)$).

On the wing the instantaneous dipole distribution $\mu(x, y, t = 4T)/(U_\infty \bar{c}]$ is constant in *x*-direction. On the wake the dipole distribution is clearly periodic in space, with dimensionless spatial period $U_\infty/(fb/2)$, which is proportional to 1/St. Also, the dipole distribution is symmetric with respect to the plane $y = 0$: $\mu(x,-y,t/T) = \mu(x,y,t/T)$. Consequently, the *x*-component (chordwise) $\gamma_x = -\partial\mu/\partial y$ of the vortex distribution is anti-symmetric: $\partial\mu/\partial y(x,-y,t/T)=-\partial\mu/\partial y(x,y,t/T)$. The *y*-component (spanwise) $\gamma_y= \partial\mu/\partial x$ of the vortex distribution is symmetric with respect to the plane $y = 0$: $\partial\mu/\partial x(x,-y,t/T)=\partial\mu/\partial x(x,y,t/T)$.

Since iso-dipole contours coincide with vortex lines, see section 3.1 and Eq. (14), in Fig. 11 the short black arrows tangential to the iso-contours, indicate the direction of the vortex lines on the wake and on the wing: $\vec{\gamma} = \vec{e}_z \times \vec{\nabla}\mu = -\frac{\partial\mu}{\partial y}\vec{e}_x + \frac{\partial\mu}{\partial x}\vec{e}_y$. In the iso-plots, the reddish regions with closed clockwise running vortex lines, forming a ring-like vortex in the plane of the wake, are regions with high values of $\mu/(U_\infty\bar{c})$, which are produced during the upstroke of the wing. The bluish regions with closed, counter-clockwise running vortex lines, are regions with negative values of $\mu/(U_\infty\bar{c})$, also a ring-like vortex of opposite direction, which are produced during the downstroke of the wing. Locally, the denser the iso-μ lines, the larger $\vec{\nabla}\mu$ and the stronger the vortex distribution. The port side of the wake features the mirror-image of the pattern observed on the starboard part of the wake.
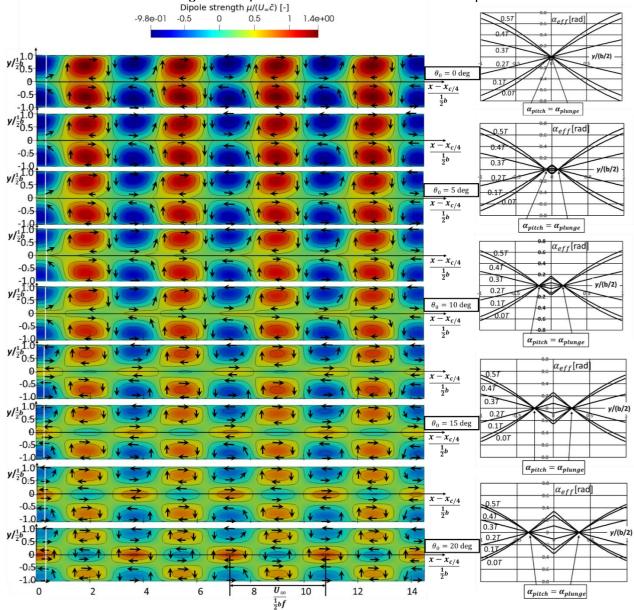

Figure 11 – Iso-contours of dipole distribution on wing and wake of simplified configuration, for conditions listed in Tables 1 and 2, for St = 0.3343, $\theta_0 = 0(2.5)20$ deg, $N = 80$, $\frac{\Delta t}{T} = 0.05$. Flow is from left to right. Iso-contour values range from $\mu/(U_\infty\bar{c}) \in [-0.98,1.4]$ in ten equal steps. Column on right shows spanwise distribution effective angle-of-attack as function of t/T for every 5 deg increment in pitch angle amplitude. Note that at time t, μ at location $x - x_{TE}$ in wake equals $\Gamma_{c/4}(y, t - (x - x_{TE})U_\infty/)$.

From the starboard side of the wing, vortex lines start and subsequently proceed in downstream direction. The more outboard starting vortex lines turn around to return to the part of the trailing edge next to the tip. Vortex lines starting from the part of the trailing edge closer to the plane of symmetry (root) do not return to the trailing edge. These vortex lines continue downstream, meandering around a sequence of regions with closed, alternatingly clock-wise and counter-clockwise running, vortex lines.

For the lower values of the pitch amplitude θ_0, vortex lines do not continue in downstream direction, but instead cross the *y*-axis (perpendicularly) to encircle the like-signed vortex region on the other side of the plane of symmetry.

The direction of the vortex lines given by the small black arrows, show that the bluish regions of low values of the dipole distribution, formed during the upstroke, at the wing tips correspond to upstream directed arrows on the starboard side and downstream directed arrows at the port side of the wing. This corresponds to tip vortices that, from a downstream point of view turn clockwise on the starboard side and counter-clockwise on the port side. For the downstroke of the wing motion, the situation is the other way around: counter-clockwise directed vortex at the starboard side and clock-wise directed vortex at the port side.

Figure 11 also illustrates that the spanwise distribution of the effective angle of attack determines the topology of the vortex distribution in the wake. Below a of θ_0 = 10 to 12.5 deg, the regions with high, similarly the ones with low, values of the dipole distribution occur in pairs, one region on the starboard side and one equal-signed region on the port-side of the wake. For higher values of the pitch amplitude θ_0, for which in the root part of the wing the effective angle of attack has the opposite sign of the effective angle of attack for the rest of the wing, the weaker and weaker, two equal-signed regions are separated more and more by a region with opposite-signed values of the dipole distribution. For pitch amplitude of θ_0 = 20 deg, the central region of the wing, with opposite-sign dipole distributions are almost as strong as the ones near the wing tips. With increasing pitch amplitudeθ_0 , the vortex wake becomes more complex in topology and the ring-like vortex regions become weaker, which results in lower lift and lower thrust.

6.1.2 Instantaneous spanwise distributions and time histories

Figure 12 (right) presents the spanwise distribution of the upwash $w_{in}(y/(b/2), t/T)$ at the lifting line for $\theta_0 = 10$ deg. At the same moments in the flapping cycle, the spanwise distribution of the circulation $\Gamma_{\frac{c}{4}}(y/0.5b), t/T)$ is given in Fig. 12-left, also for θ_0 = 10 deg. During the whole cycle the central (root) part of the lifting line carries positive circulation, while the wing tip portions carry negative circulation during the downstroke part of the cycle and positive circulation during the upstroke part of the cycle. Clearly, the evolution of the distribution mostly follows that of the effective angle of attack, see Fig. 4. The circulation is maximal in magnitude around spanwise location $y/(b/2)$ = $\pm$ 0.75 during downstroke (around t/T = 0.5) and upstroke (around t/T = 0.0/1.0).
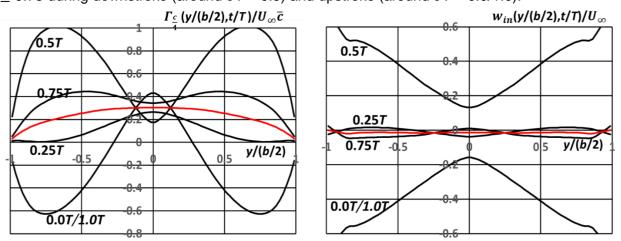

Figure 12 - Left: Spanwise distribution circulation $\Gamma_{c/4}(y/(b/2), t/T)$. Right: Spanwise distribution induced upwash $w_{in}(y/(b/2), t/T)$ at lifting line. Conditions listed in Tables 1 and 2, St = 0.3343, θ_0 = 10 deg, N = 80, $\frac{\Delta t}{T} = 0.05$. Shown are distributions at five instants in 4th cycle of motion. Upstroke: $t/T \in$ (0.75,1.0/0.0,0.25), downstroke: $t/T \in$ (0.25,0.5/0.5,0.75). Both functions are symmetric with respect to $y/(b/2)$ = 0. Red curve: Left: cycle-averaged spanwise distributions of circulation lifting line; Right: upwash induced at lifting line.

As expected, near the wing tips the distribution of the circulation appears to tend to a square-root type of behavior. Note that the distributions of $\Gamma_{\frac{c}{4}}(y/0.5b), t/T)$ are directly related to cross-sections $(x - x_{TE})/0.5b$ = constant of the iso-contours of the plot of the dipole distribution for θ_0 = 10 deg in Fig. 11. At time t the corresponding location in the wake of the wing is $x_{TE} + U_\infty t$.

Figure 12 shows that the induced upwash is mostly in phase with the circulation, i.e., the sign of the two distributions is equal over almost the entire span of the lifting line except in the root region. That indicates, as follows from the Kutta-Joukowski Theorem, that the drag force will be negative, i.e., the wing sections are generating thrust along most of the span of the wing, except at the root.

Furthermore, note that the amplitude of the unsteady distributions of circulation and upwash, with respect to the cycle-averaged distribution are quite large. Also, note that similar to the distribution of the effective angle of attack α_{eff} the distributions of circulation and that of the induced upwash intersect each other at $|y/(b/2)| \approx 0.17$, i.e., at these two points the value of effective angle of attack, circulation and induced upwash are invariant with respect to time.

Figure 13 presents, for (St = 0.3343, θ_0 = 10 deg), the temporal evolution of the circulation $\Gamma_{c/4}(y, t)$ of the lifting line and the upwash $w_{in}(y, t)$, induced at two points on the lifting line, i.e., at the root y = 0 and at point $y/(0.5b)$ = 0.75 near the wing tip. Clearly the solution becomes harmonic after the initial flapping cycle. As also clear from Fig. 12 showing the full spanwise distribution for the fourth cycle, at $y/(0.5b)$ = 0.75 the circulation and the upwash are almost in phase: i.e., when the circulation is positive/negative, the upwash is also positive/negative. In the root region, for $y/(0.5b)$ = 0. The circulation and the upwash are out of phase. This implies that, since the induced drag is proportional to the product of circulation and upwash, that the contribution to the induced drag will be negative, corresponding to thrust, over most of the four cycles calculated. Note that the temporal evolution of the circulation presented in Fig. 13 corresponds to the dipole distribution along the traverses $y/(0.5b)$ =0.0 (dashed line) and $y/(0.5b)$ = 0.75 (solid line) in Fig. 11, for the case of θ_0 = 10 deg.
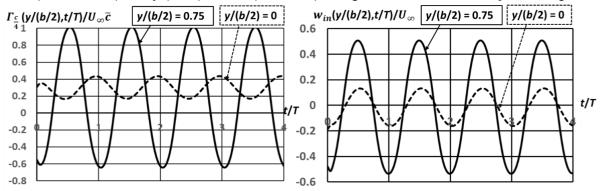

Figure 13 – Temporal evolution of circulation $\Gamma_{\bar{c}/4}(y, t)$ (left) and upwash $w_{in}(y, t)$ (right) for simplified configuration, at root y = 0 (dashed line) and near tip $y = \frac{3}{4}\frac{b}{2}$ (solid line). Conditions listed in Table 1 and 2, θ_0 = 10 deg, N = 80, $\frac{\Delta t}{T}$ = 0.05. Plot contains results for four flapping cycles.
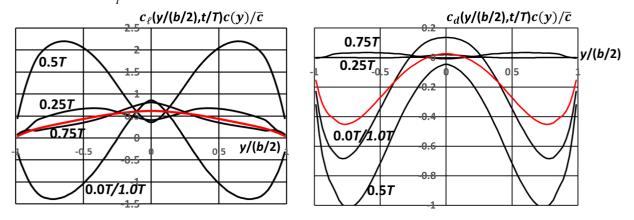

Figure 14 – Left: Spanwise distribution section wing loading $c_\ell(y/(b/2), t/T)c(y)/\bar{c}$. Right: Spanwise distribution section axial loading $c_d(y/(b/2), t/T)c(y)/\bar{c}$. Red curves: Cycle-averaged values. Lifting line method of simplified configuration, for conditions listed in Table 1 and Table 2, θ_0 = 10 deg, N = 80, $\frac{\Delta t}{T}$ = 0.05. Shown are distributions at five moments in 4th cycle. Upstroke: $t/T \in$ (0.75,1.0/0.0,0.25), downstroke: $t/T \in$ (0.25,0.5/0.5,0.75).

Figure 14 presents the spanwise distribution of the (lift) loading $c_\ell(y/(b/2), t/T)c(y)/\bar{c}$ (left) and the spanwise distribution of the axial (drag) loading $c_d(y/(b/2), t/T)c(y)/\bar{c}$ (right) at five moments in the fourth cycle of the flapping motion. Clearly, the sectional lift is directly proportional to the distribution of the circulation of the lifting line, see Fig. 12. During the whole cycle, the wing loading is positive and highest in magnitude during the downstroke, while during the upstroke the wing loading is negative but lower in magnitude. The results in a cycle-averaged distribution of the load that is positive during the whole cycle. Note that the amplitude of the distribution with respect to the cycle-averaged value is quite large.

The sectional induced drag is proportional to the product of upwash and circulation, which results in a more complicated distribution. However, because in the outboard parts ($y/(0.5b) > \approx 0.17$) of the wing the circulation and the upwash are in phase, and circulation and upwash have mostly the same sign, the result is that the sectional induced drag is negative, i.e., along almost the entire length of the lifting line the stream wise component of the force corresponds to sectional thrust. Note that during downstroke (around $t/T = 0.5$) and during upstroke (around $t/T = 0.0/1.0$) most sectional thrust is on the outer, wing-tip, parts of the wing, most during downstroke. At the present combination of parameters ($\gamma_1, \gamma_0, \theta_1, \theta_0, \varphi, \text{St}, \alpha_0, a_0$, see Table 1) during part of the cycle, the root part of the wing experiences drag.

Figure 14 also presents the cycle-averaged quantities: $\overline{c_\ell(y/(b/2), t/T)}c(y)/\bar{c}$, the spanwise distribution of the cycle-averaged wing loading (lift) and $\overline{c_d(y/(b/2), t/T)}c(y)/\bar{c}$, the cycle-averaged axial (drag) loading. The cycle-averaged lift distribution is highest in the mid-section of the wing, positive all along the lifting line, with the distribution decreasing smoothly to zero towards the wing tips. It appears that for the present wing shape and flapping/pitching parameters, at the wing tips $y/(b/2) = \pm 1$, the spanwise lift distribution is nearly elliptic, i.e., showing a $\sqrt{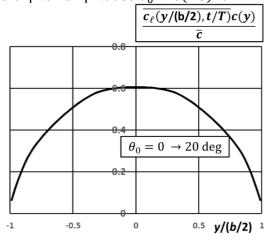1 - (\frac{y}{b/2})^2}$ behavior. Figure 14 demonstrates that during the cycle the wing loading varies considerably, from -1.4 to 2.2 at the ¾-semi-span position, where the cycle-averaged value equals 0.3, i.e., there is a large dynamic effect of the flapping on the aerodynamic wing loads.

The spanwise distribution of the cycle-averaged thrust is positive for most part of the cycle, all along the span of the lifting line, with a peak value at $\frac{y}{b/2} \approx \pm \frac{3}{4}$. In the root section lower, negative, thrust values (drag) are experienced by the flapping wing. Also, the thrust (negative drag) varies considerably during the cycle, with the highest values at the ¾-semi-span location. Here the cycle-average thrust coefficient amounts to 0.45, with excursions to 1 and -0.15.

For the present conditions the span-integrated, cycle-averaged, lift amounts to $\overline{C_L}$ = 0.4583. The span-integrated, cycle-averaged thrust amounts to $\overline{C_T}$ = 0.2237.

6.1.3 Spanwise distributions cycle-averaged load and drag (-thrust) coefficients

For St = 0.3343, Fig. 15 presents $\overline{c_\ell(y/(b/2), t)}c(y)/\bar{c}$, the spanwise distribution of the cycle-averaged wing loading (lift) and of $\overline{c_d(y/(b/2), t)}c(y)/\bar{c}$, the cycle-averaged axial (drag) loading, for the whole range of pitch amplitudes $\theta_0 = 0(2.5)20$.
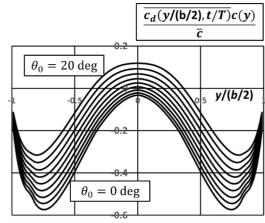
Figure 15 – Left: Spanwise distribution cycle-averaged section wing loading $\overline{c_\ell(y/(b/2), t/T)}c(y)/\bar{c}$. Right: Spanwise distribution cycle-averaged section axial loading $\overline{c_d(y/(b/2), t/T)}c(y)/\bar{c}$. Lifting line method of simplified configuration, for conditions listed in Table 1 and Table 2, St = 0.3343, $\theta_0 = 0(2.5)20$ deg, $N = 80$, $\frac{\Delta t}{T} = 0.05$.

It is noted that the cycle-averaged values $\overline{f(t)}$ are obtained from the temporal values $f(t)$ by applying the midpoint quadrature rule, for the n-th cycle with I sample points:

$$\overline{f(t)} \equiv \frac{1}{T}\int_{nT}^{(n+1)T} f(t)dt \approx \frac{1}{T}[\frac{1}{2}(t_2 - t_1)f(t_1) + \sum_{i=2}^{I-1}(t_{i+1} - t_i)f(t_i) + \frac{1}{2}(t_I - t_{I-1})f(t_I)], \qquad (50)$$

with $t_1 = nT$, $t_I = (n + 1)T$ and $\sum_{i=1}^{I-1}(t_{i+1} - t_i) = T$.

The cycle-averaged lift (load) distribution $\overline{c_\ell(y/(b/2), t)}c(y)/\bar{c}$, is highest in the mid-section of the wing, with the distribution decreasing smoothly to zero at the wing tips, in a square-root-type of fashion, as already noted in Fig. 14. The spanwise distribution of the cycle-averaged wing loading does not depend on the pitch amplitude θ_0, only on the Strouhal number. This can be deduced from the formulation of the unsteady lifting-line theory, presented in section 3.

Furthermore, the spanwise distribution of the cycle-averaged circulation $\overline{\Gamma_{c/4}(y/0.5b), t/T)}$, as well as the distribution of the cycle-averaged upwash $\overline{w_{in}(y/0.5b), t/T)}$, only depend on Strouhal number St, not on the pitch amplitude θ_0.

The spanwise distribution of the cycle-averaged sectional drag (thrust), involving the product of circulation and upwash, depends on both Strouhal number St and pitch amplitude θ_0, as can be deduced form Eq. (49). Here, for St = 0.3343, the spanwise distribution of $\overline{c_d(y/(b/2), t/T)}c(y)/\bar{c}$ varies smoothly with pitch amplitude θ_0, at any spanwise location decreasing stepwise with the stepwise pitch amplitude increasing from $\theta_0 = 0$ deg to $\theta_0 = 20$ deg. It appears that, for $\theta_0 < 7.5$ deg, the cycle-average thrust is positive along the whole lifting line, while for higher pitch amplitudes θ_0 an increasing part of the root section is subjected to drag, with a value of 0.12 at the root for $\theta_0 = 20$ deg.

6.1.4 Evolution overall lift and thrust coefficients

For St = 0.3343, Fig. 16 presents the time-dependent lift coefficient $C_L(t)$ and the time-dependent drag (negative of thrust) coefficient $C_D(t)$ of the wing, i.e., the value obtained by integrating the results presented in Fig. 14 with respect to space along the span of the wing. Given the values at the midpoints of the discretisation of the lifting line, the midpoint quadrature rule has been used to obtain the integrated values. Results are shown for the whole range of pitch amplitudes: $\theta_0 = 0(2.5)20$.
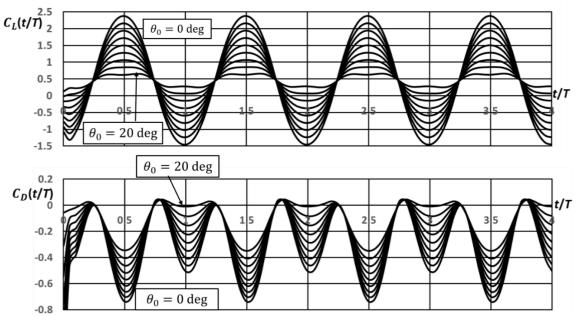

Figure 16 – Upper: Temporal lift coefficient $C_L(t/T)$. Lower: Temporal drag coefficient $C_D(t/T)$. Lifting line method of simplified configuration, for conditions listed in Table 1 and Table 2, St = 0.3343, $\theta_0 = 0(2.5)20$ deg, $N = 80$, $\frac{\Delta t}{T} = 0.05$.

Both the lift and the drag coefficients become harmonic after the first cycle of the flapping motion. For the lower values of the pitch amplitude θ_0, the amplitude of the lift coefficient is largest, with an amplitude of 2.0 for $\theta_0 = 0$, which decreases with increasing θ_0. For $\theta_0 = 10$ deg this amplitude of the temporal variation of the lift coefficient has decreased to 1.0. For still higher pitch amplitudes,

peaks in the temporal distribution flatten out and the variation with time decreases to an amplitude of 0.2. At the highest pitch amplitudes of $\theta_0 > 15$ deg, the lift coefficient is positive during the whole cycle. Note that, though the amplitude of $C_L(t/T)$ very much depends on the pitch amplitude θ_0, like the spanwise distribution of the cycle-averaged wing load. The cycle-averaged value $\overline{C_L}$ of the time-dependent overall lift coefficient $C_L(t)$ does not vary with pitch amplitude θ_0.

The evolution of the drag coefficient is also harmonic, but in a form somewhat more complex than the lift coefficient. This can be understood by realising that the drag is proportional to the product of the distribution of the circulation of the lifting line and the upwash distribution, induced at the lifting line, by the wake dipole distribution. The latter depends linearly on the circulation distribution of the lifting line at the same moment in time and at all earlier moments in time. That yields a first harmonic at double the frequency of the frequency of the flapping/pitching motion [21].
The maximum value of the harmonic drag/thrust coefficient decreases with increasing pitch amplitude: the peak amplitude of the thrust coefficient $(-C_D(t/T))$ equals about 0.7 in absolute value at $\theta_0 = 0$, which decreases to 0.35 at $\theta_0 = 20$ deg

6.1.5 Time-averaged overall lift and thrust coefficients, dependence on θ_0 and St

Figure 17 presents the cycle-averaged lift coefficient $\overline{C_L} = \overline{C_L(t/T)}$ and the cycle-averaged thrust coefficient $\overline{C_T} = -\overline{C_D(t/T)}$ as function of the Strouhal number St, for pitch amplitude $\theta_0 = 0(2.5)20$ deg. The Strouhal numbers considered were St = {$10^{-3}, 10^{-2}, 0.025, 0.05, 0.1, 0.15, 0.19, 0.24, 0.3, 0.3343$}. Figure 17 shows that the unsteady-lifting-line method predicts a mean lift coefficient that, like the cycle-averaged load distribution, does not depend on the pitch angle. For small values of St the lift coefficient asymptotes to $\overline{C_L} = 0.5507$, the drag coefficient to $\overline{C_D} = -0.0003$. For steady flow, lifting-line theory provides the lift coefficient for an AR = 7.3358 wing with $\alpha_0 = -5$ deg, at zero angle of attack, from [26]:
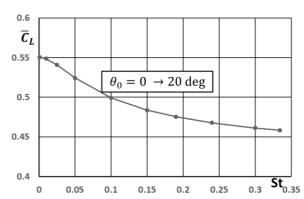
$$C_L = \frac{a_0}{1+\frac{a_0}{\pi e AR}}(\alpha - \alpha_0),$$

with $a_0 = 2\pi$ the sectional lift slope and e the span efficiency. For $e = 1$, it follows that $C_L = 0.5483$, a value close to $\overline{C_L} = 0.5507$ determined in Fig. 17 for St $\to$ 0. For the induced drag coefficient $C_{D,in}$, the lifting-line theory provides [26]:

$$C_{D,in} = \frac{C_L^2}{\pi e AR}.$$

So, for the present wing it follows $C_{D,in} = 0.0131$. Figure 17 gives for St = 10^{-3} a value of $\overline{C_D}$ between -0.00014 and -0.0014, i.e., a small thrust rather than a drag.

The overall lift coefficient $\overline{C_L}$ decreases with increasing Strouhal number, which is due to the shorter wave length of the time-dependent dipole (vortex) distribution on the wake, which equals $\frac{U_\infty}{f} = \frac{2h_0}{St}$. The upwash w_{in} induced by the wake at the lifting line decreases with decreasing St.
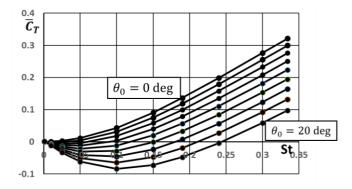

Figure 17 – Left: Mean lift coefficient $C_L = \overline{C_L(t/T)}$ vs Strouhal number St, for pitch amplitude $\theta_0 = 0(2.5)20$ deg. Right: Mean thrust coefficient $C_T = -\overline{C_D(t/T)}$ vs Strouhal number St, for pitch amplitude $\theta_0 = 0(2.5)20$ deg. St = {$10^{-3}, 10^{-2}, 0.025, 0.05, 0.1, 0.15, 0.19, 0.24, 0.3, 0.3343$}. Lifting line method of simplified configuration, for conditions listed in Tables 1 and Table 2, $\theta_0 = 0(2.5)20$ deg, $N = 80$, $\frac{\Delta t}{T} = 0.05$.

Finally, included in Fig. 17 is the overall, cycle-averaged, thrust coefficient $\overline{C_T}$ as function of Strouhal number St, for the full range of pitch amplitudes θ_0. The results show that the cycle-averaged (mean)

span-integrated thrust coefficient is positive for higher Strouhal numbers and lower pitch amplitudes θ_0. There is also a range of combinations (St, θ_0) for which the overall thrust turns into drag: the lower St, the lower the pitch amplitude should be in order to retain thrust.

6.1.6 Knoller-Betz / von Kármán – Burgers effect

Figure 18 presents a snapshot at $t/T = 4$ of the distribution of the spanwise component $\gamma_y(y/(0.5b), t)/U_\infty$ of the wake vortex distribution along the traverse $y/(0.5b) = 0.75$, $z = 0$, from trailing-edge to 14 wing semi-spans downstream. This traverse has been chosen because it passes through the spanwise location at which the thrust is highest, e.g., see Figs. 14 and 15. Figure 18 illustrates the harmonic character of the wake vortex distribution, with an in time constant amplitude and nearly equal magnitude of positive (clock-wise sense of rotation) and negative (counter-clockwise sense of rotation) peak values.
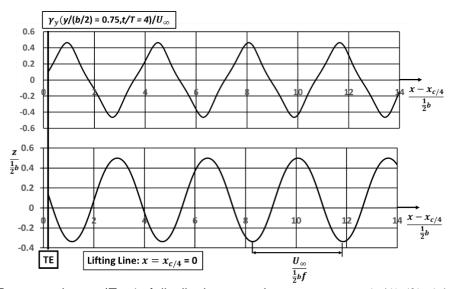

Figure 18 - Top: snapshot at $t/T = 4$ of distribution spanwise component $\gamma_y(y/(0.5b), t)/U_\infty$ vortex distribution along traverse $y/(0.5b) = 0.75$, $z = 0$, from trailing-edge to 14 semi-spans downstream. Bottom: estimate cross-section wake vortex sheet, at same instant, in plane $y/(0.5b) = 0.75$. Lifting-line model of simplified configuration, for the conditions listed in Tables 1 and 2, $\theta_0 = 10$ deg, $N = 80$, $\frac{\Delta t}{T} = 0.05$.

Furthermore, note that between the peaks and the valleys of the distribution of $\gamma_y(y/(0.5b), t)/U_\infty$ the slope of the distribution of γ_y/U_∞ is almost constant, namely $\frac{1}{U_\infty}\frac{\partial \gamma_y}{\partial x} \approx \pm 1$.

Figure 18 also presents the corresponding cross-section of the wake vortex sheet in the plane $y/(0.5b) = 0.75$, at instant $t/T = 4$. The shape of the wake vortex sheet in the present unsteady-lifting-line method is the plane $z = 0$. The estimate of the true state is obtained from the assumption that the wake vortex sheet is formed at the trailing edge of the wing and subsequently, like the dipole distribution, is convected with velocity $U_\infty \vec{e}_x$ in downstream direction. Therefore, at time t, the wake vortex sheet is determined by the motion of the trailing edge at all earlier moments in time. As clear from Fig. 18, the wake vortex sheet and the distribution of the spanwise component γ_y of the vortex distribution are 180 deg out of phase. This leads to the situation that γ_y is maximal negative (counter-clockwise sense) at the peaks and maximal positive (clockwise sense) at the valleys of the wavy wake vortex sheet. Precise such a configuration of the wake is used to explain the generation of thrust by flapping (plunging/pitching) wings through the so-called Knoller-Betz effect [9], [30], [31], also called the von Kármán-Burgers effect [32], in which the self-induced flow inside the reverse von-Kármán-vortex-street type of wake is jet-like. This downstream-directed jet results in an upstream-directed reaction, i.e., thrust.

In the present study the wake is represented by a flat (transpiration) surface in the plane $z = 0$. This implies that, since the vortex distribution is situated in this plane, the self-induced velocity of the wake, will not be jet-like nor wake-like. Instead, the upwash generated at the lifting line by this simplified wake geometry causes, through the Kutta-Joukowski Theorem, the thrust experienced by the lifting line.

6.2 Results Experiments

The experimental results were post-processed in several ways in order to reveal the shape of the wake, as well as the evolution in time of the different vorticity components. Figure 19 shows iso-surfaces of the vorticity magnitude, coloured by the value of the spanwise vorticity. It appears that the wing generates negative spanwise vorticity during the upstroke and positive spanwise vorticity during the downstroke. This is similar to the prediction by the numerical method in Fig. 11. Specifically, the experimental results match the predicted results for cases with $\theta_0 < 10$ deg. For higher pitch amplitudes, a change of sign in vorticity closer to the wing would be expected, but this is not seen in the experimental results. The limit of $\theta_0 < 10$ matches the expected value of the pitch amplitude, as observed in a previous study [28].
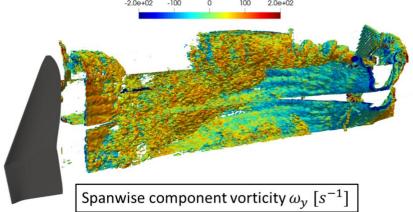

Figure 19 - Visualisation flow measurements for $U_\infty = 6 \text{ m/s}$ (see Table 3), facing pressure side of wing. Shown are iso-volumes of vorticity magnitude $|\vec{\omega}| \in= [100,300] \, [1/s]$ with intervals of 50 [1/s]. The contours are coloured with value of spanwise vorticity. Note that the wake is sinusoidal and represents a single period of the wing flapping cycle: starting with the upstroke at the far right, moving through zero-position in the middle of the wake.

Figure 20 shows a cross-section, at the plane at $y = 220$ mm, of the acquired vector volume. This figure further illustrates that indeed a free shear layer with positive spanwise component of the vorticity is generated during the downstroke and negative vorticity during the upstroke.

The cross-section of the field of the y-component of the vorticity ω_y in Fig. 20 reveals about one wave length of the shear layer of the wake. The shape of the shear layer resembles the one shown in Fig. 18. In the lower part of Fig. 20, the wake vortex sheet of Fig. 18, is repeated, now with the vortex sheet coloured with the value of the spanwise component of the wake vortex distribution. The lower part of Fig. 20, obtained from the unsteady lifting-line method, clearly resembles the upper part obtained from the PIV results.
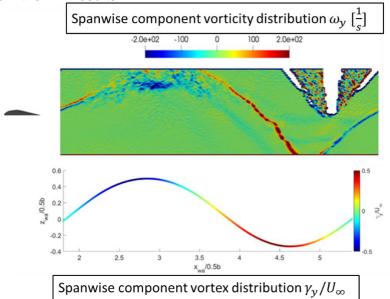

Figure 20 – Top: Spanwise (y-)component of vorticity measured for $U_\infty = 6 \text{ m/s}$ (see Table 3) on plane at $y = 220 \text{ mm}$, which is approximately at half semi-span of wing. Bottom: similar cross-section approximated wake vortex sheet with strength spanwise component wake vortex distribution indicated by colour.

Furthermore, in the upper figure, ω_y is predominantly negative (counter-clockwise) near the top of the shear layer and predominantly positive (clockwise) near the valley in the shear layer, again resembling the configuration presented in lower figure of Fig. 20 and in Fig. 18. This makes clear that in the present experimental results, indeed, the reverse von-Kármán vortex street is evident and that via the Knoller-Betz/von Kármán-Burgers effect it is clear that, without determining the force itself directly, the flapping wing experiences a thrust force.

Figure 21 shows the development of the tip vortex with distance from the trailing edge of the wing, or equivalently, as evolution in time, since the flow features in a plane at x = constant in the wake at time t, were generated at time $t - (x - x_{TE})/U_\infty$. In the wake the sign of the vorticity in the tip vortex depends on location, i.e., also on the time it was generated at the trailing edge. The topology revealed in Figs. 19 and 21, agrees with the predicted results in section 6.2. However, an important difference can also be observed: during the upstroke the tip vortex seems to interact with the tip vortex of opposite sign generated during the preceding part of the flapping cycle. This results in the mushroom-shaped cross-section of the vortical structure seen in the third cutting plane from the left.
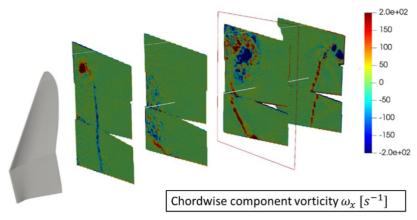

Figure 21 - Tip vortex for different moments in flapping cycle for $U_\infty = 6$ m/s (see Table 3), visualized through chordwise component vorticity ω_x. Cutting planes: from right to left: upstroke, halfway upstroke, end of upstroke and downstroke. Adapted from [21].

7 Concluding Remarks

Prandtl's lifting-line, approximate, theory for the incompressible, inviscid, irrotational, steady flow about thin, mildly-cambered, high-aspect-ratio wings has been extended for application to flapping wings. In the extended theory the circulation of the wing, i.e., of the lifting line, is time-dependent. The theory is formulated in terms of a time-dependent dipole distribution $\mu(x,y,t)$ on a planar, stationary wake reference surface. The planar surface, z = 0, consists of the wing, with attached to its trailing edge, a semi-infinite wake surface also in the plane z = 0.

On the wing the dipole distribution is approximated by a spanwise distribution $\Gamma_{c/4}(y, t)$ along the ¼-chord line, continued to the trailing edge by a chordwise-constant distribution $\mu(x,y,t) = \Gamma_{c/4}(y, t)$. Therefore, the trailing edge carries a dipole distribution identical to the dipole distribution along the lifting line at the 1/4-chord line. This formulation is identical to Prandtl's lifting line formulation, with the lifting-line along the 1/4-chord line, however, with the difference that in Prandtl's theory for steady flow, the chord-wise-constant dipole distribution is continued to infinity downstream. The dipole distribution on the wake surface is the continuation of the dipole distribution on the wing. In the case of unsteady flow, at time t, the wake dipole distribution is determined in terms of $\Gamma_{c/4}(y, t^*)$ generated at the trailing edge at earlier times, which subsequently is convected onto the wake surface. The unsteady-lifting-line method includes the newly derived Kutta-Joukowski Theorem for unsteady flow and the Kutta trailing-edge condition for unsteady flow.

The resulting unsteady lifting-line method has been applied to a flapping wing like the Robird wing. The method predicts: (i) the topology of the vortical wake of the flapping wing; (ii) the spanwise distributions of transient (and cycle-averaged) sectional lift (wing load) and sectional axial force (thrust); (iii) the transient (and cycle-averaged) overall lift and overall thrust, for a number of pitching amplitudes and a number of Strouhal numbers. These numerical results provide insight in the trends in topology of the vortical wake, lift and thrust experienced by the flapping wing due to variation in

pitch amplitude and Strouhal number. It has been demonstrated that the spanwise distribution of cycle-averaged sectional circulation, sectional lift (load) and upwash, as well as cycle-averaged overall lift, depend on Strouhal number St, but do not depend on pitch amplitude θ_0, while the spanwise distribution of cycle-averaged sectional thrust and of cycle-averaged overall thrust depend on both Strouhal number and pitch amplitude θ_0.

Prediction of required power and of propulsive efficiency of flapping flight forms future work.

A number of these findings, specifically on wake topology, were subsequently validated with the help of PIV measurements. The PIV measurements indicate that the unsteady-lifting-line method captures two important flow phenomena accurately: tip vortices of opposite sign for the up- and downstroke, i.e., vorticity generated at the trailing edge changes sign from upstroke to downstroke. Also, the predictions by the unsteady-lifting-line method gives further credibility to previously performed measurements on the deformation and pitching motion of the wing during the flight of the Robird.

The computational method, however, does not account for the three-dimensional transient shape of the wake of the Robird. In addition, the PIV measurements are still to be used to predict thrust and lift of the wing from the measured three-dimensional velocity field. This will be the subject of future work.

Acknowledgments

Contact Author Email Address

mailto: h.w.m.hoeijmakers@utwente.nl

Copyright Statement

References

[1] Folkertsma GA, Straatman W, Nijenhuis N, Venner CH and Stramigioli S. Robird: a robotic bird of prey. *IEEE Robotics and Automation Magazine*, Vol. 24, No. 3, pp. 22–29, 2017. https://doi.org/10.1109/MRA.2016.2636368.

[2] Gerdes J, Holness A, Perez-Rosado A, Roberts L, Greisinger A, Barnett E, Kempny J, Lingam D, Yeh CH, Bruck HA and Gupta SK. Robo Raven: A flapping-wing air vehicle with highly compliant and independently controlled wings. *Soft Robotics*, Vol. 1, No. 4, pp. 275–288, 2014. https://doi.org/10.1089/soro.2014.0019.

[3] Send W, Fischer M, Jebens K, Mugrauer R, Nagarathinam A, and Scharstein F. Artificial hinged-wing bird with active torsion and partially linear kinematics. *28th Congress of the International Council of the Aeronautical Sciences 2012, ICAS*2012, Vol. 2, pp. 1148–1157, 2012.

[4] Karasek M, Muijres FT, Wagter CD, Remes BD and de Croon GC. A tailless aerial robotic flapper reveals that flies use torque coupling in rapid banked turns. *Science*, Vol. 361, No. 6407, pp. 1089–1094, 2018. https://doi.org/10.1126/science.aat0350.

[5] Wood RJ, The first takeoff of a biologically inspired at-scale robotic insect. *IEEE Transactions on Robotics*, Vol. 24, No. 2, pp. 341–347, 2008. https://doi.org/10.1109/TRO.2008.916997.

[6] Thielicke W, Kesel A and Stamhuis E. Reliable force predictions for a flapping-wing micro air vehicle: A "vortex-lift" approach. *International Journal of Micro Air Vehicles*, Vol. 3, No. 4, pp. 201–215, 2011. https://doi.org/10.1260/1756-8293.3.4.201.

[7] Hubel TY, Hristov NI, Swartz SM and Breuer KS. Time-resolved wake structure and kinematics of bat flight. *Experiments in Fluids*, Vol. 46, No. 5, pp. 933–943, 2009. https://doi.org/10.1007/s00348-009-0624-7.

[8] Muijres FT, Johansson LC and Hedenström A. Leading edge vortex in a slow-flying passerine. *Biology Letters*, Vol. 8, No. 4, pp. 554–557, 2012. https://doi.org/10.1098/rsbl.2012.0130.

[9] Jones KD, Dohring CM and Platzer M F. Experimental and computational investigation of the Knoller-Betz effect. *AIAA Journal*, Vol. 36, No. 7, pp. 1240–1246, 1998. https://doi.org/10.2514/2.505.

[10] Rayner, J. M. V., "A vortex theory of animal flight. Part 1. The vortex wake of a hovering animal," *Journal of Fluid Mechanics*, Vol. 91, No. 4, 1979, pp. 697–730. URL https://www.cambridge.org/core/product/identifier/S0022112079000410/type/journal_article.

[11] Spedding G. The wake of a Kestrel (Falco Tinnunculus) in flapping flight. *Journal of Experimental Biology*, Vol. 127, No. 1, pp. 59–78, 1987.

[12] Li J and Wu ZN. Unsteady lift for the Wagner problem in the presence of additional leading/trailing edge vortices. *Journal of Fluid Mechanics*, Vol. 769, pp. 182–217, 2015. https://doi.org/10.1017/jfm.2015.118.

[13] Mulder JL, Hoeijmakers HWM. Computational and experimental investigation into flapping wing propulsion. *Proceedings 54th AIAA Aerospace Sciences Meeting*, *AIAA Science and Technology Forum and Exhibition (SciTech*2016*),* San Diego, California, USA, AIAA Paper 2016-0802, 33 pages, 2016.

[14] Brentjes A, Hoeijmakers HWM. Experimental investigation into wake flapping wing robotic bird. *Proceedings AIAA AVIATION* 2017, 35th *AIAA Applied Aerodynamics Conference*, Denver, Colorado, USA, AIAA Paper 2017-3409, 25 pages, 2017.

[15] Gijsman F, Hoeijmakers HWM. Experimental study of flow in wake robotic bird. *Proceedings AIAA AVIATION Forum*, 2018 *Applied Aerodynamics Conference*, Atlanta, Georgia, USA, AIAA Paper 2018-3175, 18 pages, 2018.

[16] Spedding GR, Rosén M and Hedenström A. A family of vortex wakes generated by a thrush nightingale in free flight in a wind tunnel over its entire natural range of flight speeds. *Journal of Experimental Biology*, Vol. 206, No. 14, pp. 2313–2344, 2003. https://doi.org/10.1242/jeb.00423.

[17] Gutierrez E, Quinn DB, Chin DD and Lentink D. Lift calculations based on accepted wake models for animal flight are inconsistent and sensitive to vortex dynamics. *Bioinspiration and Biomimetics*, Vol. 12, No. 1, 2017. https://doi.org/10.1088/1748-3190/12/1/016004.

[18] Hartman SA, Hoeijmakers HWM, Musters R. Experimental investigation of flow about wing of robot bird. *Proceedings 50th AIAA Aerospace Sciences Meeting including the New Horizons Forum and Aerospace Exposition*, Nashville, TN, USA, AIAA Paper 2012-0055, 19 pages, 2012.

[19] Groot Koerkamp L, de Santana LD, Hoeijmakers HWM, Venner CH. Investigation into wake of flapping wing of robotic bird. *Proceedings AIAA AVIATION Forum*, 2019 *Applied Aerodynamics Conference*, Dallas, Texas, USA, AIAA Paper 2019-3582, 22 pages. eISBN: 978-1-62410-589-0, 2019.

[20] de Santana LD, Sanders MP, Venner CH and Hoeijmakers HWM. The UTwente aeroacoustics wind tunnel upgrade. *Proceedings AIAA AVIATION Forum*, 2018 *AIAA/CEAS Aeroacoustics Conference*, Atlanta, Georgia, USA, AIAA Paper 2018-3136, 12 pages, 2018.

[21] Groot Koerkamp L, de Santana LD, Hoeijmakers HWM, Venner CH. Development and experimental validation of lifting-line-based model for a robotic bird. *Proceedings AIAA AVIATION Forum*, 2022 *Applied Aerodynamics Conference*, Chicago, Illinois, USA, AIAA Paper 2022-tbd, 22 pages, 2022.

[22] Huckriede KW, Koop AH, Hospers JM, Hoeijmakers HWM. Finite-volume method with transpiration boundary conditions for flow about oscillating wings. *Conference Proceedings 48th AIAA Aerospace Sciences Meeting,* Orlando, Florida, USA. AIAA Paper 2010-0866, 20 pages, 2010.

[23] Hoeijmakers HWM. Panel methods for aerodynamic analysis and design. *AGARD-FDP/VKI Special Course on Engineering Methods in Aerodynamic Design of Aircraft.* AGARD Report R-783 Chapter 5, 1991.

[24] Prandtl L. Tragflügeltheorie. *Nachrichten der Gesellschaft der Wissenschaften zu Göttingen, Mathematisch-physikalische Klasse*, pp. 451-477, 1918. See also *Application of modern hydrodynamics to aeronautics.* NACA Report No. 116, 1921.

[25] Milne-Thomson LM. *Theoretical hydrodynamics*. 5th edition, Dover Publications, 1968.

[26] Anderson Jr JD. *Fundamentals of aerodynamics*. 6th edition, McGraw-Hill Education,2017.

[27] Katz J. and Plotkin A. Low-Speed Aerodynamics. 2nd edition, Cambridge University Press, 2001. P. 384, Eq. (13.36).

[28] Gies SH., Folkertsma GA., Stramigioli S and Venner CH. Ornithopter flight dynamics: measurement and analysis of the Robird's flapping wing Ornithopter Flight Dynamics: Measurement and Analysis of the Robird's Flapping Wing. http://purl.utwente.nl/essays/74077, 2017.

[29] Westerweel J and Scarano F. Universal outlier detection for PIV data. *Experiments in Fluids*, Vol. 39, No. 6, pp. 1096–1100. https://doi.org/10.1007/s00348-005-0016-6, 2005.

[30] Knoller R. Die Gesetze des Luftwiderstandes. *Flug- und Motortechnik* (Wien), Vol. 3, No. 21, pp. 1– 7.2, 1909.

[31] Betz A. Ein Beitrag zur Erklärung des Segelfluges. *Zeitschrift für Flugtechnik und Motorluftschiffahrt*, Vol. 3, pp. 269–273, 1912.

[32] von Kármán Th and Burgers JM. *Aerodynamic Theory*. Volume II General Aerodynamic Theory - Perfect Fluids. Durand WF (editor-in-chief). Julius Springer, Berlin. 1935. ISBN-13: 978-3-642-89628-6. DOI: 10.1007/978-3-642-91485-0. p. 308, Fig. 105.